

A simplified electro-chemical lithium-ion battery model applicable for in-situ monitoring and online controlling

Yuxuan Gu^{a,1}, Qixin Chen^{a,*,2}, Yuanbo Chen^{a,3}, Hongye Guo^{a,4} and Kedi Zheng^{a,5}

^aDepartment of Electrical Engineering, Tsinghua University, Beijing 100084, China.

ARTICLE INFO

Keywords:

discrete-time state-space representations
electro-chemical model
lithium-ion battery
model simplification
state estimation

ABSTRACT

The penetrations of lithium-ion batteries in transport, energy and communication systems are increasing rapidly. A meticulous model applicable for precise in-situ monitoring and convenient online controlling is in sought to bridge the gap between research and applications. This paper proposes a simplified electro-chemical model and its discrete-time state-space realization derived from the pseudo-two-dimensional model. The solution-phase migration and solid-phase diffusion dynamics with varying parameters are captured and rigorous mathematical expressions of reaction rate distribution and terminal voltage are derived. A simulation framework including initializing, stabilizing and closed-loop correcting schemes with low computation cost are designed. Numeric experiments on different types of batteries in various operating scenarios are conducted for validation.

1. Introduction

Lithium-ion batteries (LIBs) have become the dominant energy source in various applications, such as electric vehicles, grid-level energy storage, etc. The advantages of an LIB include high power and energy density, long lifespan, high efficiency, low self-discharge, and non-memory effect. With the widespread usage, security and economic concerns of LIBs are rapidly raising as well. LIBs are monitored and controlled by the battery management system (BMS) to achieve safe, efficient and reliable operation. The BMS estimates the state of charge (SOC), state of power (SOP) and state of health (SOH) of LIBs based on the battery model and output measurements, and then generates control actions.

For advanced BMS, the underlying battery model should be with the following features. First, it should be able to provide information of internal states like potentials, Li^+ concentrations, reaction rates, etc. for meticulous management. Second, it can be converted to state-space representations easily for online controlling. Last, it should be simple with low requirements on the processor and memory since an LIB

pack can contain hundreds of cells to be modeled.

Existing LIB models can be categorized into three groups: data-driven, empirical, and electro-chemical. Data-driven models (black-box models) are usually fitted on experimental data by statistical methods to predict battery dynamics [1]. The equivalent circuit model (ECM) is a representative of empirical models, which uses a series of resistors and capacitors to mimic the battery [2, 3, 4]. The electro-chemical model (EM) uses a set of partial differential and algebraic equations (PDAEs) to depict chemical and physical processes at the micro-scale inside the battery cell [5]. Comparing with the former two groups, EMs can give mechanism interpretations of the battery and are adaptive to a wide range of scenarios. However, EMs are usually complex and hard to be transformed into state-space models for controlling, which impede their widespread usage.

The representative of EMs is pseudo-two-dimensional (P2D) model, which was proposed by Doyle et al. [5] and later became the original source of subsequent models. Based on the porous electrode theory and concentrated solution theory, the P2D model mainly depicts the diffusion/migration of ions in the electrode/electrolyte and the intercalation at

*Corresponding author

ORCID(s): 0000-0002-3733-8641 (Q. Chen)

the solid-solution interface. Since the seminal work of [5], a plenty of works refined the original P2D model, such as incorporating the double layer capacitance [6, 7, 8], constant-phase-element dynamics [7], aging factors [8], varying parameters [9, 10], etc. However, these refinements further increase the complexity. To enable practical usage of EMs, a plethora of works put efforts on model reduction techniques, which can be categorized into three approaches: numerical, analytical, and hybrid.

Numerical approaches focus on developing high-efficient computation methods for PDAEs in the model. Mathematically, PDAEs are spatially discretized into ordinary differential and algebraic equations (ODAEs) and then solutions are obtained iteratively. For the discretization process, finite-difference [11], control-volume formulation (CVF) [9], Crank-Nicolson method [12], Forward Time-Central Space approximation [13] and asymptotic reduction [14] have been proposed. [15] used proper orthogonal decomposition (POD) to solve the whole model, which was also used by [16] to calculate solid-phase potentials. [17] developed the solving scheme based on the singular perturbation and averaging theory. However, numerically reduced models are still with high orders (30-100 orders). In addition, the deficiency of a control-oriented view disables the model for online implementations.

Analytical approaches aim to find approximate expressions for concerned variables in the model, which are obtained by intuitive assumptions or rigorous derivations. For approximating the solution-phase Li^+ concentration, constant [18, 19], parabolic or cubic polynomials [20, 21, 22, 23, 24, 25] and residue grouping [16, 26, 27] are commonly used. Sinusoidal and exponential functions were also tried in [28, 29]. For approximating the solid-phase surface Li^+ concentration, many works start from simplifying its transfer

function (TF) and then conduct state-space realizations. The Padé approximation was first introduced by Forman et al. [30] and then be widely used [10, 16, 22, 26, 28, 31], which obtains a rational polynomial approximation of the original TF by conducting Taylor expansion at $s = 0$. Since Padé approximations only hold for low frequency, rational polynomial coefficients are obtained by minimizing the frequency response error over a wide frequency band [32, 33]. In [21, 34], coefficients are obtained by directly fitting on variable sequences in the time-domain. Anyhow, after state-space realizations, these models can be viewed as a combination of several first-order processes. Some research used the realization algorithm (xRA) to directly obtain the state-space representation [7, 35]. The xRA can generate a discrete-time state-space realization with similar unit-pulse response to the original system. Volume-averaging model was also widely adopted, which assumes a polynomial distribution of Li concentrations along the r -axis [23, 24, 25, 29, 36, 37]. Since the original TF contains \sqrt{s} term, fractional-order models was also investigated in some work [38, 33]. For the reaction rate, constant, step-wise linear [33], parabolic polynomials [39, 40, 41] and cubic polynomials [42] were used for approximation.

Hybrid approaches treat some part of the model with numerical methods while the remained part with analytical methods, e.g., applying Padé approximation for solid-phase and finite-difference for solution-phase [43, 44].

After reviewing aforementioned research and attempting several high-cited models, some problems emerge to be solved. First, for solution-phase Li^+ concentrations, existing works mainly focused on the spatial distribution. Under the view of developing a control-oriented model, time variations modeling and discrete-time state-space realization need consummation. Second, for solid-phase Li^+ concentra-

tions, we find that the simplified state-space representations obtained by Padé approximation, response or time-series optimization, or xRA, coupled with non-uniform reaction rate model, are likely to suffer from oscillations. Developing an accurate but robust method is necessary for practical usage. Third, for the reaction rate distribution, polynomial approximations used by existing models are based on intuitive assumptions and not adaptive to various scenarios. As the key to in-situ monitoring, degradation prediction and lumped-states estimation (SOC, SOP, SOH) [45], a rigorous mathematical formula is in sought. Forth, for the whole cell, a model considering coupled electrical, chemical, physical, and thermal dynamics along with varying parameters sensitive to the concentration or temperature, and a framework covering the full cycle of simulation, including the initialization, stabilization, and closed-loop correction, are in need for real-world applications.

In order to bridge gaps mentioned above, a high-fidelity reduced-order model along with the simulation framework are proposed in this work. Parameters sensitive to temperatures or concentrations are extracted and then modeled by Arrhenius law and empirical formulas. The solution-phase migration is simplified by two coupled first-order inertial processes derived from the mass conservation and Fick's law. For the solid-phase diffusion, by attempting various methods, we finally arrive at using a first-order inertial process with proper time constant to achieve a balance between the accuracy, stabilization and simplicity. For the reaction rate distribution, the conceptual content is fully considered and a rigorous mathematical expression without intuitive assumptions is derived. The above models are integrated to obtain a discrete-time state-space realization of the whole cell. For full-cycle simulation of the cell, the initialization, stabilization and closed-loop correction schemes, which are com-

posed of simple calculations or optimizations with low computation cost, are designed. For validation, the proposed model is compared with the full-order P2D model, extended single particle (ESP) model and a high-cited model proposed by Han et al. [21, 40] in various scenarios for different kinds of cells.

The contributions of this work are four fold.

- A simplified electro-chemical lithium-ion battery model along with the discrete-time state-space realization are proposed. The developed model is adaptive to a wide range of scenarios and cell types.
- A simulation framework including the initialization, stabilization and closed-loop correction with low computation cost is designed for easy implementations in real-world applications.
- The proposed model and framework are validated by comprehensive case studies for different scenarios and cell types, and their superiority is revealed.
- The in-situ monitoring and online controlling can be realized at the same time based on this work, which provides opportunities for degradation analysis and meticulous management of batteries in practice.

The rest of this paper is organized as follows: Section 2 develops a lithium-ion battery model. Section 3 designs the framework for full-cycle simulation. Section 4 presents case studies. Section 5 draws conclusions.

2. A simplified electro-chemical model

Typically, cylindrical or prismatic battery cells have a sandwich structure divided by three domains: negative electrode, separator and positive electrode, the diagram is shown in Fig. 1.

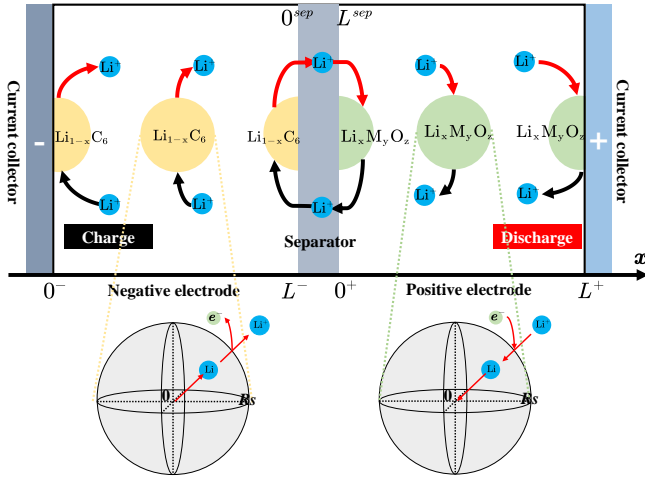


Figure 1: Diagram of an LIB cell sandwich.

Electrodes are porous with the solid-phase composed of active materials (AMs), polymer matrix, conductive filler additive and solution-phase filled by electrolytes. Positive AMs are usually transition metal oxide, e.g., nickel-cobalt-manganese oxide ($\text{LiNi}_x\text{Co}_y\text{Mn}_z\text{O}_2$, NCM) and iron phosphate (LiFePO_4 , LFPO). Negative AMs are usually graphite (C_6). The separator is a perforated micro-plastic that insulates electrons but allows ions to pass. Electrolytes are usually non-aqueous solvent mixture with low electronic conductivity (e.g., a mixture of propylene carbonate, ethylene carbonate and dimethyl carbonate) and a single salt (e.g., LiPF_6 , LiClO_4).

During charging, lithium-ions de-intercalate from negative AMs, migrate in electrolytes through the separator, and intercalate into positive AMs. Meanwhile, electrons transport through the current collector from negative to positive in the external circuit. During discharging, ions and electrons transport in reverse directions. The chemical reaction formula is written as $\text{Li}_x\text{X} + \text{Li}_{1-x}\text{Y} \xrightleftharpoons[\text{discharge}]{\text{charge}} \text{X} + \text{LiY}$, where X and Y refer to positive and negative AMs.

2.1. Parameters

Parameters can be categorized into five groups: geometric, transport, material, thermal and auxiliary. Parameter no-

tations and meanings are listed in Appendix A. To improve fidelity, parameters sensitive to concentrations or temperatures (D_s , D_e , κ , k_r) are modeled independently.

We assume D_s varies linearly with the solid-phase bulk-averaged Li^+ concentration $\bar{c}_s(x, t)$ (mol/m^3):

$$D_s(x, t) = k_{D_s}(t) \frac{\bar{c}_s(x, t)}{c_{s, \max}} + b_{D_s}(t). \quad (1)$$

Assume k_{D_s} and b_{D_s} obey the Arrhenius law when temperatures vary. Denote the activation energy of these two coefficients by $E_{A, k_{D_s}}$ and $E_{A, b_{D_s}}$ (J/mol), the reference values by $k_{D_s, \text{ref}}$ and $b_{D_s, \text{ref}}$, the reference temperature by T_{ref} (K), the battery temperature by $T(t)$ (K), they are computed by:

$$\begin{aligned} k_{D_s}(t) &= \exp\left(-E_{A, k_{D_s}}(1/T(t) - 1/T_{\text{ref}})/R\right) k_{D_s, \text{ref}}, \\ b_{D_s}(t) &= \exp\left(-E_{A, b_{D_s}}(1/T(t) - 1/T_{\text{ref}})/R\right) b_{D_s, \text{ref}}. \end{aligned} \quad (2)$$

Empirical expressions of D_e and κ for the PC-EC-DMC mixture, which is widely used as the electrolyte solvent in commercial LIBs, are adopted [20, 23, 46, 47, 48]. Denote the solution-phase Li^+ concentrations by $c_e(x, t)$ (mol/m^3):

$$D_e(x, t) = 10^{-8.43 - \frac{54}{T(t) - 229 - 0.005c_e(x, t)} - \frac{2.2}{10^4}c_e(x, t)}. \quad (3)$$

$$\begin{aligned} \kappa(x, t) &= \frac{c_e(x, t)}{10^4} \left(\left(\frac{0.494}{10^6} c_e^2(x, t) + \frac{0.668}{10^3} c_e(x, t) - 10.5 \right) \right. \\ &\quad + \left(\frac{-8.86}{10^{10}} c_e^2(x, t) - \frac{1.78}{10^5} c_e(x, t) + 0.074 \right) T(t) \\ &\quad \left. + \left(\frac{2.8}{10^8} c_e(x, t) - \frac{6.96}{10^5} \right) T^2(t) \right). \end{aligned} \quad (4)$$

Reaction rate coefficients k_r also obey the Arrhenius law when temperatures vary, denote the activation energy by E_{A, k_r} ,

(J/mol), the reference value by $k_{r,\text{ref}}$:

$$k_r^\pm(t) = \exp\left(-\frac{E_{A,k_r^\pm}}{R}\left(\frac{1}{T(t)} - \frac{1}{T_{\text{ref}}}\right)\right) k_{r,\text{ref}}^\pm \quad (5)$$

The rest parameters are assumed to be constant values. It is noteworthy that in the long-term, some parameters will vary with the battery degradation. However, this work mainly focuses on real-time simulations, degradation identification and analysis will be investigated in the following research.

2.2. Solution-phase migration model

Denote the pore-wall-flux at the surface of AMs by $j_n(x, t)$ (mol/m²/s), the migration of lithium-ions in the electrolyte along the thickness follows Fick's second law:

$$\varepsilon_e^\pm \frac{\partial c_e(x, t)}{\partial t} = \frac{\partial}{\partial x} (D_e^{\text{eff}}(x, t) \frac{\partial c_e(x, t)}{\partial x}) + a_s^\pm (1 - t_+^0) j_n(x, t). \quad (6)$$

where $D_e^{\text{eff}}(x, t)$ is corrected by the Bruggeman relation for porous structure electrodes, $D_e^{\text{eff}} = D_e(\varepsilon_e)^p$. For notation simplicity, D_e^{eff} is replaced by D_e in the following text.

Using parabolic polynomials to approximate the spatial distribution of $c_e(x, t)$, $c_e(x, t)$ can be expressed by $a_e^-(t)x^2 + b_e^-(t)$, $a_e^+(t)(x - L^+)^2 + b_e^+(t)$ and $a_e^{\text{sep}}(t)x + b_e^{\text{sep}}(t)$ for the negative electrode, positive electrode and separator, respectively. Integrate the LHS and RHS of (6) along the x-axis over the electrode domain yields:

$$\frac{1}{A^\pm} \frac{\partial \int_{0^\pm}^{L^\pm} A^\pm \varepsilon_e^\pm c_e(x, t) dx}{\partial t} = D_e(x, t) \frac{\partial c_e(x, t)}{\partial x} \Big|_{0^\pm}^{L^\pm} + \frac{(1 - t_+^0)}{F} \int_{0^\pm}^{L^\pm} a_s^\pm F j_n(x, t) dx. \quad (7)$$

Physically, the numerator in the LHS of (7) refers to the total quantity of lithium-ions in the solution-phase of the electrode domain, denoted by $Q_e^\pm(t)$ here. Substituting $c_e(x, t)$ into $Q_e^\pm(t)$ yields $Q_e^\pm(t) = A^\pm \varepsilon_e^\pm \left(\frac{1}{3} a_e^\pm(t) (L^\pm)^3 + b_e^\pm(t) L^\pm \right)$.

By Faraday's law, the second term in the RHS of (7) equals to the difference between the solid-phase current density, denoted by $i_s(x, t)$ (A/m²), at two sides of the electrode. Substituting boundary conditions of $i_s(x, t)$ and expressions of c_e into (7) yields:

$$\frac{dQ_e^\pm(t)}{dt} = 2A^\pm L^\pm D_e^\pm(t) a_e^\pm(t) \mp \frac{(1 - t_+^0)}{F} I(t). \quad (8)$$

where $D_e^+(t) = D_e(0^+, t)$, $D_e^-(t) = D_e(L^-, t)$. Based on continuities of the Li⁺ concentration and flux at interfaces between different domains, the following formulas are derived:

$$\frac{L^- D_e(L^-, t) a_e^-(t)}{D_e(0^{\text{sep}}, t)} + \frac{L^+ D_e(0^+, t) a_e^+(t)}{D_e(L^{\text{sep}}, t)} = 0. \quad (9)$$

$$\begin{aligned} a_e^-(t) L^- (L^- + \frac{D_e(L^-, t)}{D_e(0^{\text{sep}}, t)} L^{\text{sep}}) + b_e^-(t) = \\ a_e^+(t) L^+ (L^+ + \frac{D_e(0^+, t)}{D_e(L^{\text{sep}}, t)} L^{\text{sep}}) + b_e^+(t). \end{aligned} \quad (10)$$

Merge $Q_e^\pm(t)$, (9), (10) into the matrix form:

$$\mathbf{L}(t) \begin{bmatrix} a_e^-(t) \\ b_e^-(t) \\ a_e^+(t) \\ b_e^+(t) \end{bmatrix} = \begin{bmatrix} 0 \\ 0 \\ Q_e^-(t)/A^- \varepsilon_e^- \\ Q_e^+(t)/A^+ \varepsilon_e^+ \end{bmatrix} \quad (11)$$

where $\mathbf{L}(t)$ in the formula above is:

$$\begin{bmatrix} \frac{D_e^-(t) L^-}{D_e(0^{\text{sep}}, t)} & 0 & \frac{D_e^+(t) L^+}{D_e(L^{\text{sep}}, t)} & 0 \\ L^- \left(L^- + \frac{D_e^-(t) L^{\text{sep}}}{D_e(0^{\text{sep}}, t)} \right) & 1 & -L^+ \left(L^+ + \frac{D_e^+(t) L^{\text{sep}}}{D_e(L^{\text{sep}}, t)} \right) & -1 \\ (L^-)^3 / 3 & L^- & 0 & 0 \\ 0 & 0 & (L^+)^3 / 3 & L^+ \end{bmatrix}$$

Then quadratic coefficients of $c_e(x, t)$, $a_e^-(t)$ and $a_e^+(t)$, can

be expressed by:

$$\begin{aligned} a_e^-(t) &= \mathbf{L}_{1,3}^{-1}(t)Q_e^-(t)/A^-\varepsilon_e^- + \mathbf{L}_{1,4}^{-1}(t)Q_e^+(t)/A^+\varepsilon_e^+, \\ a_e^+(t) &= \mathbf{L}_{3,3}^{-1}(t)Q_e^-(t)/A^-\varepsilon_e^- + \mathbf{L}_{3,4}^{-1}(t)Q_e^+(t)/A^+\varepsilon_e^+. \end{aligned} \quad (12)$$

where $\mathbf{L}_{1,3}^{-1}(t)$ represents the element on the 1st row and 3rd column of the matrix $\mathbf{L}^{-1}(t)$ and so forth.

Since only cations (i.e., Li^+) are involved in the reaction, the mass conservation of anions always holds. By electro-neutrality, the total quantity of cations in the solution phase, $Q_e^0 = (\varepsilon_e^- A^- L^- + \varepsilon_e^+ A^+ L^+)c_{e,0} = Q_e^-(t) + Q_e^+(t)$, is constant at any instance in time. Substituting it into (8) yields:

$$\begin{aligned} \frac{dQ_e^-(t)}{dt} &= 2A^- L^- D_e^-(t) \left(\frac{\mathbf{L}_{1,3}^{-1}(t)}{A^-\varepsilon_e^-} - \frac{\mathbf{L}_{1,4}^{-1}(t)}{A^+\varepsilon_e^+} \right) Q_e^-(t) \\ &\quad + 2A^- L^- D_e^-(t) \frac{\mathbf{L}_{1,4}^{-1}(t)Q_e^0}{A^+\varepsilon_e^+} + \frac{(1-t_+^0)}{F} I(t), \\ \frac{dQ_e^+(t)}{dt} &= 2A^+ L^+ D_e^+(t) \left(\frac{\mathbf{L}_{3,4}^{-1}(t)}{A^+\varepsilon_e^+} - \frac{\mathbf{L}_{3,3}^{-1}(t)}{A^-\varepsilon_e^-} \right) Q_e^+(t) \\ &\quad + 2A^+ L^+ D_e^+(t) \frac{\mathbf{L}_{3,3}^{-1}(t)Q_e^0}{A^-\varepsilon_e^-} - \frac{(1-t_+^0)}{F} I(t). \end{aligned} \quad (13)$$

For notation simplicity, (13) is represented by:

$$\tau_e^\pm(t) \frac{dQ_e^\pm(t)}{dt} = -Q_e^\pm(t) + K_{Q_e}^\pm(t). \quad (14)$$

where $\tau_e^\pm(t)$ and $K_{Q_e}^\pm(t)$ can be derived from (13).

Now the time variations of Q_e^\pm are modeled by two coupled first-order inertial processes. Once Q_e^\pm are obtained, $c_e(x, t)$ at any point in x-axis can be calculated by (11).

2.3. Solid-phase diffusion model

In operation, lithium-ions diffuse along the radial direction of AMs and react at the solid-solution interface. To capture dynamics of the solid-phase Li^+ concentration, denoted by $c_s(x, r, t)$ (mol/m³), AMs are modeled as a collection of spherical particles and the diffusion of Li^+ is assumed to

obey Fick's second law:

$$\frac{\partial c_s(x, r, t)}{\partial t} = \frac{D_s(x, t)}{r^2} \frac{\partial}{\partial r} (r^2 \frac{\partial c_s(x, r, t)}{\partial r}), \quad (15)$$

with boundary conditions:

$$\left. \frac{\partial c_s(x, r, t)}{\partial r} \right|_{r=0} = 0, \quad \left. \frac{\partial c_s(x, r, t)}{\partial r} \right|_{r=R_s} = -\frac{j_n(x, t)}{D_s}. \quad (16)$$

There are plenty of works on simplifying the solid-phase diffusion model as reviewed above. However, by attempting existing methods, two challenges still remain. First, for in-situ monitoring of the battery, a series of points have to be selected along the thickness direction and the diffusion model have to be constructed at every point independently, which means the model should be reduced as simple as possible. Second, if considering the non-uniform reaction rate, we find the approximated TF whose time constants are obtained from Padé approximation or frequency response optimization are likely to suffer from oscillations. Same situations also happen for xRA and volume-averaging methods. After investigation, we find this problem may be caused by a too small time constant. Thus, a simple first-order inertial process with tuned time constants is used to realize a trade-off between accuracy, stabilization, and simplicity.

Moving r^2 in the RHS of (15) to the LHS and integrating both sides along the r-axis yields:

$$\frac{1}{4\pi} \frac{\partial \int_0^{R_s} 4\pi r^2 c_s(x, r, t) dr}{\partial t} = D_s(x, t) R_s^2 \left. \frac{\partial c_s(x, r, t)}{\partial r} \right|_{R_s}. \quad (17)$$

Physically, $\int_0^{R_s} 4\pi r^2 c_s(x, r, t) dr$ refers to the total quantity of Li^+ in the particle, which can also be represented by the bulk-averaged Li^+ concentration, denoted by $\bar{c}_s(x, t)$:

$$\int_0^{R_s} 4\pi r^2 c_s(x, r, t) dr = \frac{4}{3} \pi R_s^3 \bar{c}_s(x, t). \quad (18)$$

Substituting (18) and (16) into (17) yields:

$$\frac{\partial \bar{c}_s(x, t)}{\partial t} = -\frac{3}{R_s} j_n(x, t). \quad (19)$$

Beside $\bar{c}_s(x, t)$, the surface Li^+ concentration denoted by $c_{ss}(x, t)$, is also concerned. Denote the difference between $c_{ss}(x, t)$ and $\bar{c}_s(x, t)$ by $w(x, t)$, the Laplace transformation of $w(x, t)$ can be derived from (15):

$$\frac{w(x, s)}{j_n(x, s)} = \frac{R_s}{D_s} \frac{1}{1 - R_s \sqrt{\frac{s}{D_s}} \coth(R_s \sqrt{\frac{s}{D_s}})} + \frac{3}{R_s} \frac{1}{s}. \quad (20)$$

Calculating the limitation of (20) at $s = 0$: $\lim_{s \rightarrow 0} \frac{w(x, s)}{j_n(x, s)} = -\frac{R_s}{5D_s}$, indicating for a constant $j_n(x, t)$, $w(x, t)$ will approach $-\frac{R_s j_n(x, t)}{5D_s(x, t)}$ gradually, $c_{ss}(x, t)$ can then be expressed by:

$$c_{ss}(x, t) = \bar{c}_s(x, t) - \frac{R_s}{5D_s(x, t)} j_n(x, t). \quad (21)$$

The transition from starting to steady states is modeled by a first-order inertial process with a time constant proportional to the ratio of radius square and diffusion rate, i.e., $\tau_s(x, t) = k_s^\pm \frac{(R_s^\pm)^2}{D_s(x, t)}$. Thus we have:

$$\tau_s(x, t) \frac{\partial w(x, t)}{\partial t} = -w(x, t) + K_w(x, t). \quad (22)$$

where $K_w(x, t) = -\frac{R_s^\pm}{5D_s(x, t)} j_n(x, t)$. Subsequently, $c_{ss}(x, t)$ can be represented by:

$$c_{ss}(x, t) = \bar{c}_s(x, t) + w(x, t). \quad (23)$$

In Padé approximation, the equivalent value of k_s^\pm is $\frac{1}{35}$. In volume-averaging method, there are two first-order processes mathematically, the equivalent values of k_s^\pm are $\frac{1}{30}$ and 0, respectively. In [21], values of k_s^\pm are 0.04356 and 0.03459. By frequency response optimization, k_s^\pm equals to 0.0214 for one first-order process or 0.0016 and 0.0356 for

two first-order processes (the frequency band is $[10^{-4}, 10^4]\text{Hz}$).

By testing above settings, we find that they suffer from oscillation commonly except for [21], which indicating a smaller k_s^\pm can bring destabilization to the model. However, a larger k_s^\pm makes the model less accurate, especially under dynamic currents. In this work, k_s^\pm is determined by experiments to realize a trade-off between accuracy and stabilization.

2.4. Reaction rate distribution model

The reaction rate is the key to determining operating region and analysing degradation states. By solving equations derived from electrical laws and chemical laws, we derive its rigorous mathematical expression in this part.

2.4.1. Electrical system

By Faraday's law, the differential of the solid-phase current is expressed by $\partial i_s(x, t)/\partial x = -a_s^\pm F j_n(x, t)$. Thus, $i_s(x, t)$ is obtained by integration:

$$i_s(x, t) = \begin{cases} -a_s^- F \int_{0^-}^x j_n(l, t) dl + I(t)/A^-, & x \in [0^-, L^-]; \\ a_s^+ F \int_x^{L^+} j_n(l, t) dl + I(t)/A^+, & x \in [0^+, L^+]. \end{cases} \quad (24)$$

By Kirchhoff's law, the sum of $i_s(x, t)$ and solution-phase current, denoted by $i_e(x, t)$ (A/m^2), always equals to $I(t)/A$. Thus, we have:

$$i_e(x, t) = \begin{cases} a_s^- F \int_{0^-}^x j_n(l, t) dl, & x \in [0^-, L^-]; \\ -a_s^+ F \int_x^{L^+} j_n(l, t) dl, & x \in [0^+, L^+]. \end{cases} \quad (25)$$

By Ohm's law, the gradient of the solid-phase potential, denoted by $\Phi_s(x, t)$ (V), is determined by:

$$\frac{\partial \Phi_s(x, t)}{\partial x} = -\frac{i_s(x, t)}{\sigma_s^{\pm, \text{eff}}}. \quad (26)$$

It is noteworthy that the solid-phase conductivity is corrected by the Bruggeman correction, $\sigma_s^{\pm, \text{eff}} = \sigma_s^{\pm} \varepsilon_s^{\pm}$. For notation simplicity, $\sigma_s^{\pm, \text{eff}}$ is replaced by σ_s^{\pm} in the following text.

The gradient of the solution-phase potential, denoted by $\Phi_e(x, t)$ (V), is composed of ohmic potential drop and concentration polarization potential:

$$\frac{\partial \Phi_e(x, t)}{\partial x} = -\frac{i_e(x, t)}{\kappa^{\text{eff}}(x, t)} - \frac{2RT(t)(t_+^0 - 1)(1 + \frac{d \ln f_{\pm}}{d \ln c_e})}{F} \frac{\partial \ln c_e(x, t)}{\partial x}. \quad (27)$$

To improve fidelity, a parabolic polynomial is used to depict the mapping between $\frac{d \ln f_{\pm}}{d \ln c_e}$ and c_e . Similarly, the solution-phase conductivity is corrected by the Bruggeman correction, $\kappa^{\text{eff}}(x, t) = \kappa(x, t) \varepsilon_e^p$. For notation simplicity, $\kappa^{\text{eff}}(x, t)$ is replaced by $\kappa(x, t)$ in the following text. Introduce $\kappa_D(x, t)$ to replace the complicated formula:

$$\kappa_D(x, t) = 2\kappa(x, t) \frac{RT(t)}{F} (t_+^0 - 1) (a_f c_e(x, t)^2 + b_f c_e(x, t) + c_f). \quad (28)$$

Denote the potential difference between the solid-phase and solution-phase by Φ_{s-e} . The gradient of Φ_{s-e} can be obtained by subtracting (27) from (26):

$$\frac{\partial \Phi_{s-e}(x, t)}{\partial x} = \begin{cases} -\frac{I(t)}{A^- \sigma^-} + a_s^- F \left(\frac{1}{\sigma^-} + \frac{1}{\kappa(x, t)} \right) \int_0^x j_n(l, t) dl \\ + \frac{\kappa_D(x, t)}{\kappa(x, t)} \frac{\partial \ln(c_e(x, t))}{\partial x}, x \in [0^-, L^-]; \\ -\frac{I(t)}{A^+ \sigma^+} - a_s^+ F \left(\frac{1}{\sigma^+} + \frac{1}{\kappa(x, t)} \right) \int_x^{L^+} j_n(l, t) dl \\ + \frac{\kappa_D(x, t)}{\kappa(x, t)} \frac{\partial \ln(c_e(x, t))}{\partial x}, x \in [0^+, L^+]. \end{cases} \quad (29)$$

In (29), $\frac{\partial \ln(c_e(x, t))}{\partial x}$ can be approximated by:

$$\frac{\partial \ln(c_e(x, t))}{\partial x} = \begin{cases} \frac{2a_e^-(t)x}{a_e^-(t)x^2 + b_e^-(t)} \approx \frac{2a_e^-(t)}{b_e^-(t)} x, x \in [0^-, L^-]; \\ \frac{2a_e^+(t)(x-L^+)}{a_e^+(t)(x-L^+)^2 + b_e^+(t)} \approx \frac{2a_e^+(t)(x-L^+)}{b_e^+(t)}, x \in [0^+, L^+]. \end{cases} \quad (30)$$

2.4.2. Chemical system

The intercalation reaction rate is determined by the Butler-Volmer equation:

$$j_n(x, t) = \frac{i_0(x, t)}{F} \left(\exp\left(\frac{\alpha_a F \eta(x, t)}{RT(t)}\right) - \exp\left(\frac{-\alpha_c F \eta(x, t)}{RT(t)}\right) \right). \quad (31)$$

where $\eta(x, t)$ (V) is the over-potential, $\eta(x, t) = \Phi_{s-e}(x, t) - U_{OCF}(x, t) - F R_f j_n(x, t)$, and i_0 is the exchange current density, $i_0(x, t) = k_r^{\pm} c_e(x, t)^{\alpha_a} (c_{s, \max}^{\pm} - c_{ss}(x, t))^{\alpha_c} c_{ss}(x, t)^{\alpha_a}$. By assuming the proportions of the anodic and cathodic directions of the total reaction are equal [49], α_a and α_c are set at 0.5. U_{OCF} (V) is the equilibrium potential of the intercalation reaction, which is determined by the solid-phase materials and denoted by $U_{OCF}(x, t) = f_{OCF}(c_{ss}(x, t)/c_{s, \max})$.

To avoid the complexity caused by the non-linearity of (31), several approximations have been proposed for simplicity, e.g., Tafel equation, linear current-potential equation, and hyperbolic sine approximation [50]. However, they are less adaptive to various scenarios. In this work, the B-V equation is linearized adaptively with the current. Denote the average pore-wall-flux by \bar{j}_n^{\pm} (mol/m²/s) and the average exchange current density by \bar{i}_0^{\pm} (A/m²), where $\bar{j}_n^{\pm}(t) = \mp \frac{I(t)}{a_s^{\pm} F A^{\pm} L^{\pm}}$ and $\bar{i}_0^{\pm}(t) = k_r^{\pm} \sqrt{\bar{c}_e^{\pm}(t) \bar{c}_{ss}^{\pm}(t) (c_{s, \max}^{\pm} - \bar{c}_{ss}^{\pm}(t))}$. Apply the first-order Taylor expansion at \bar{j}_n^{\pm} to (31):

$$\eta(x, t) = a_{j_n}(t) j_n(x, t) + b_{j_n}(t). \quad (32)$$

In the formula above,

$$a_{j_n}(t) = \frac{RT(t)}{\bar{i}_0^\pm(t)} \frac{\sqrt{\frac{F^2(\bar{j}_n^\pm(t))^2}{4(\bar{i}_0^\pm(t))^2} + 1} + \frac{F\bar{j}_n^\pm(t)}{2\bar{i}_0^\pm(t)}}{\frac{F\bar{j}_n^\pm(t)}{2\bar{i}_0^\pm(t)} \sqrt{\frac{F^2(\bar{j}_n^\pm(t))^2}{4(\bar{i}_0^\pm(t))^2} + 1} + \frac{F^2(\bar{j}_n^\pm(t))^2}{4(\bar{i}_0^\pm(t))^2} + 1}. \quad (33)$$

According to the definition of $\eta(x, t)$, we have $\Phi_{s-e}(x, t) - U_{OCP}(x, t) - FR_f^\pm j_n(x, t) = a_{j_n} j_n(x, t) + b_{j_n}$. Calculating the partial differential of Φ_{s-e} yields:

$$\frac{\partial \Phi_{s-e}(x, t)}{\partial x} = (a_{j_n}(t) + FR_f^\pm) \frac{\partial j_n(x, t)}{\partial x} + \frac{\partial U_{OCP}(x, t)}{\partial x}. \quad (34)$$

For in-situ monitoring of the battery cell, we evenly select four points in each electrode, their coordinates are denoted by $x_1^\pm, x_2^\pm, x_3^\pm, x_4^\pm$. Then $U_{OCP}(x, t)$ can be approximated by a cubic polynomial: $U_{OCP}^\pm(x, t) = a_P^\pm(t)x^3 + b_P^\pm(t)x^2 + c_P^\pm(t)x + d_P^\pm(t)$. The coefficients can be solved by $U_{OCP}(x, t)$ at the selected four points. Thus, we have $\frac{\partial U_{OCP}(x, t)}{\partial x} = 3a_P(t)x^2 + 2b_P(t)x + c_P(t)$.

2.4.3. Mathematical Representation

Denote the integration of $j_n(x, t)$ over the electrode by $J_n(x, t)$, i.e., $J_n^-(x, t) = \int_0^x j_n^-(l, t) dl$ for the negative electrode and $J_n^+(x, t) = \int_x^{L^+} j_n^+(l, t) dl$ for the positive electrode. Considering (34) and (29) yields

$$\mp k_1^\pm(t) J_n^\pm(x, t) \pm k_2^\pm(t) \frac{\partial^2 J_n^\pm(x, t)}{\partial x^2} + k_3^\pm(t) x^2 + k_4^\pm(t) x + k_5^\pm(t) = 0. \quad (35)$$

In the formula above, $k_1^\pm(t) = a_s^\pm F \left(\frac{1}{\sigma_s^\pm} + \frac{1}{\bar{k}^\pm(t)} \right)$, $k_2^\pm(t) = a_{j_n}^\pm(t) + FR_f^\pm$, $k_3^\pm(t) = -3a_P^\pm(t)$, $k_4^\pm(t) = 2 \frac{a_e^\pm(t) \bar{k}_D^\pm(t)}{b_e^\pm(t) \bar{k}^\pm(t)} - 2b_P^\pm(t)$, $k_5^\pm(t) = -\frac{I}{A-\sigma_s^\pm} - c_P^\pm(t)$, $k_5^+(t) = -\frac{I}{A^+\sigma_s^+} - c_P^+(t) - 2 \frac{a_e^+(t) \bar{k}_D^+(t)}{b_e^+(t) \bar{k}^+(t)} L^+$.

Boundary conditions of (35) are given by:

$$\begin{aligned} J_n^-(0^-, t) &= 0, & J_n^-(L^-, t) &= \frac{I(t)}{a_s^- A^- F}, \\ J_n^+(0^+, t) &= -\frac{I(t)}{a_s^+ A^+ F}, & J_n^+(L^+, t) &= 0. \end{aligned} \quad (36)$$

The rigorous expression of $j_n(x, t)$ can be obtained then:

$$\begin{aligned} j_n^\pm(x, t) &= \pm m_1^\pm(t) \sqrt{\frac{k_1^\pm(t)}{k_2^\pm(t)}} \exp \left(-\sqrt{\frac{k_1^\pm(t)}{k_2^\pm(t)}} x \right) \\ &\mp m_2^\pm(t) \sqrt{\frac{k_1^\pm(t)}{k_2^\pm(t)}} \exp \left(\sqrt{\frac{k_1^\pm(t)}{k_2^\pm(t)}} x \right) - \frac{2k_3^\pm(t)}{k_1^\pm(t)} x - \frac{k_4^\pm(t)}{k_1^\pm(t)}. \end{aligned} \quad (37)$$

where $m_{1,2}^\pm(t)$ are solved by (36).

2.5. Output model

Commonly, the measurable output of the battery cell includes the terminal voltage and surface temperature.

2.5.1. Terminal voltage

The terminal voltage, denoted by $V(t)$ (V) equals to the difference between the solid-phase potentials at the positive and negative electrode boundary minus the ohmic potential drop in current collectors. Since the solid-phase potential Φ_s equals to the sum of Φ_{s-e} and Φ_e , we have:

$$V(t) = \Phi_{s-e}(L^+, t) + \Phi_e(L^+, t) - \Phi_{s-e}(0^-, t) - \Phi_e(0^-, t) - R_c I(t). \quad (38)$$

Φ_{s-e} at the boundary can be calculated by B-V equation:

$$\begin{aligned} \Phi_{s-e}(L^+/0^-, t) &= U_{OCP}^\pm(L^+/0^-, t) + FR_f^\pm j_n(L^+/0^-, t) + \\ &\frac{2RT(t)}{F} \ln \left(\frac{F j_n(L^+/0^-, t)}{2i_0(L^+/0^-, t)} + \sqrt{\left(\frac{F j_n(L^+/0^-, t)}{2i_0(L^+/0^-, t)} \right)^2 + 1} \right). \end{aligned} \quad (39)$$

Potential drop in the solution phase is composed of the ohmic potential and polarization potential, refer to the first and second terms in the RHS of (27). The polarization potential drop of each domain is given by:

$$\Delta\Phi_{e,1}^{\pm,\text{sep}}(t) = -\bar{\kappa}_D^{\pm,\text{sep}} \ln\left(\frac{c_e(L^{\pm,\text{sep}}, t)}{c_e(0^{\pm,\text{sep}}, t)}\right). \quad (40)$$

Substituting $j_n^{\pm}(x, t)$ into (25) to obtain $i_e(x, t)$, the ohmic potential drop in the solution-phase can be derived by integrating $i_e(x, t)$:

$$\begin{aligned} \Delta\Phi_{e,2}^{\pm}(t) = & \pm \frac{a_s^{\pm} F}{\bar{\kappa}^{\pm}(t)} (-m_1^{\pm}(t) \sqrt{\frac{k_2^{\pm}(t)}{k_1^{\pm}(t)}} (\exp\left(-\sqrt{\frac{k_1^{\pm}(t)}{k_2^{\pm}(t)}} L^{\pm}\right) - 1) \\ & + m_2^{\pm}(t) \sqrt{\frac{k_2^{\pm}(t)}{k_1^{\pm}(t)}} (\exp\left(\sqrt{\frac{k_1^{\pm}(t)}{k_2^{\pm}(t)}} L^{\pm}\right) - 1) \pm \frac{k_3^{\pm}(t)}{3k_1^{\pm}(t)} (L^{\pm})^3 \\ & \pm \frac{k_4^{\pm}(t)}{2k_1^{\pm}(t)} (L^{\pm})^2 \pm (\frac{k_5^{\pm}(t)}{k_1^{\pm}(t)} + \frac{2k_2^{\pm}(t)k_3^{\pm}(t)}{k_1^{\pm}(t)^2}) L^{\pm}). \end{aligned} \quad (41)$$

In the separator domain, $\Delta\Phi_{e,2}^{\text{sep}}(t) = -\frac{L^{\text{sep}} I(t)}{\bar{\kappa}^{\text{sep}}(t) A^{\text{sep}}}$. Thus, the total solution-phase potential drop is:

$$\Phi_e(L^+, t) - \Phi_e(0^-, t) = \Sigma(\Delta\Phi_{e,1}^{\pm,\text{sep}}(t) + \Delta\Phi_{e,2}^{\pm,\text{sep}}(t)). \quad (42)$$

Substituting (42) into (38) and $V(t)$ can be obtained.

2.5.2. Cell temperature

Temperatures can infect the battery operating significantly. A lumped-thermal model is developed to predict the cell temperature based on the following assumptions: First, the temperature distribution is uniform at any instant in time, i.e., the surface temperature always equal to the core temperature [51]. Second, the enthalpy mixing and phase-change heat are neglected [52]. Third, the reversible entropy change of reaction is neglected [53].

Denote the ambient temperature by T_{amb} and the reac-

tion heat generation rate by $Q_h(t)$, the energy conservation equation is given by:

$$mC_p \frac{dT(t)}{dt} = h_c A_s (T_{\text{amb}} - T(t)) + Q_h(t). \quad (43)$$

In the formula above, $Q_h(t)$ is calculated by:

$$\begin{aligned} Q_h(t) = & -F(A^- \int_{0^-}^{L^-} a_s^- j_n(x, t) U_{OCP}^-(x, t) dx \\ & + A^+ \int_{0^+}^{L^+} a_s^+ j_n(x, t) U_{OCP}^+(x, t) dx) - I(t)V(t). \end{aligned} \quad (44)$$

For notation simplicity, (43) can be represented by:

$$\tau_T \frac{dT(t)}{dt} = -T + K_T(t). \quad (45)$$

where $\tau_T = mC_p/h_c A_s$ and $K_T(t) = Q_h(t)/h_c A_s + T_{\text{amb}}$.

3. The closed-loop simulation framework

3.1. Discrete-time state-space realization

To enable online controlling, a discrete-time state-space representation is necessary. During operating, the applied current and ambient temperature sequences are sampled by zero-order hold circuit, i.e., the input is assumed to be galvanostatic and thermostatic every time step.

In this work, the solution-phase migration, solid-phase diffusion and thermal model contain the first-order inertial process. Denote the time-stamp at the start and end of the current period by t_{k-1} and t_k , denote the current time interval by $T_{s,k} = t_k - t_{k-1}$. Between t_{k-1} and t_k , the applied current and ambient temperature are assumed to be constant. At t_{k-1} , D_s , D_e , κ , κ_D and $k_r^{\pm}(t_k)$ are updated by (1), (3), (4), (28) and (5). Then, $j_n^{\pm}(x, t)$, $x = x_1^{\pm}, \dots, x_4^{\pm}$ is calculated by (37) and assumed to be constant. Next, inertial states at t_k

are updated by:

$$\begin{aligned}
 Q_e^\pm(t_k) &= Q_e^\pm(t_{k-1}) \exp\left(-\frac{T_{s,k}}{\tau_e^\pm(t_{k-1})}\right) + K_{Q_e}^\pm(t_{k-1}) \\
 &\quad \left(1 - \exp\left(-\frac{T_{s,k}}{\tau_e^\pm(t_{k-1})}\right)\right). \\
 \bar{c}_s(x, t_k) &= \bar{c}_s(x, t_{k-1}) - \frac{R_s^\pm T_{s,k}}{3} j_n^\pm(x, t_{k-1}), x = x_1^\pm, \dots, x_4^\pm. \\
 w(x, t_k) &= w(x, t_{k-1}) \exp\left(-\frac{T_{s,k}}{\tau_w(x, t_{k-1})}\right) + K_w(x, t_{k-1}) \\
 &\quad \left(1 - \exp\left(-\frac{T_{s,k}}{\tau_w(x, t_{k-1})}\right)\right), x = x_1^\pm, \dots, x_4^\pm. \\
 T(t_k) &= T(t_{k-1}) \exp\left(-\frac{T_{s,k}}{\tau_T(t_{k-1})}\right) + K_T(t_{k-1}) \\
 &\quad \left(1 - \exp\left(-\frac{T_{s,k}}{\tau_T(t_{k-1})}\right)\right).
 \end{aligned} \tag{46}$$

It is noteworthy that $K_{Q_e}^\pm$, $K_w(x)$, K_T are also assumed to be constant between t_{k-1} and t_k . Such assumptions are made based on the fact that the varying of chemical reactions and parameters is negligible in a short time. Based on (11), (23) and (38), $c_e(x, t_k)$, $c_{ss}(x, t_k)$ ($x = x_1^\pm, \dots, x_4^\pm$) and $V(t_k)$ can be calculated. Then above steps are repeated for the next time interval.

3.2. Initializing process

The initialization for the simulation of a real battery is presented in this part. First, request the manufacturing and material information of the battery from the manufacturer and set values of parameters in Table B.1. Second, set the operating region of the battery: the low cut-off and high cut-off voltage V_{\min} and V_{\max} . By full-cycle low-current charge and discharge in the operating region, total capacity of the battery cell Q_c (mAh) can be obtained. Then the stoichiometry region of AMs in the positive and negative electrode can

be obtained by solving the non-linear equations below:

$$\begin{cases}
 U_{OCP}^+(y_0^+) - U_{OCP}^-(y_1^-) = V_{\max}, \\
 U_{OCP}^+(y_1^+) - U_{OCP}^-(y_0^-) = V_{\min}, \\
 A^+ L^+ c_{s,\max}^+ \epsilon_s^+(y_1^+ - y_0^+) = \frac{3.6Q_c}{F}, \\
 A^- L^- c_{s,\max}^- \epsilon_s^-(y_1^- - y_0^-) = \frac{3.6Q_c}{F}.
 \end{cases} \tag{47}$$

where y_0^\pm and y_1^\pm refer to the minimum and maximum stoichiometry, respectively. Third, the SOC-OCV curve can be derived:

$$OCV = f_{OCP}^+(y_1^+ - SOC(y_1^+ - y_0^+)) - f_{OCP}^-(y_0^- + SOC(y_1^- - y_0^-)). \tag{48}$$

Fourth, determine the initial states of the given battery cell. By measuring the open circuit voltage (OCV) of the cell, the initial SOC can be obtained by interpolation in the SOC-OCV curve. The solid-phase states are then initialized at:

$$\begin{aligned}
 c_{ss}(x_i^+, 0) &= \bar{c}_s(x_i^+, 0) = c_{s,\max}^+(y_1^+ - SOC_0(y_1^+ - y_0^+)), \\
 c_{ss}(x_i^-, 0) &= \bar{c}_s(x_i^-, 0) = c_{s,\max}^-(y_0^- + SOC_0(y_1^- - y_0^-)), \\
 w(x_i^+, 0) &= 0, w(x_i^-, 0) = 0, i = 1, 2, 3, 4.
 \end{aligned} \tag{49}$$

The solution-phase states are directly initialized at:

$$Q_e^\pm(0) = A^\pm L^\pm \epsilon_e^\pm c_{e,0}. \tag{50}$$

The cell temperature $T(0)$ is initialized at the ambient temperature.

3.3. Stabilizing algorithm

By experiments, we find that smaller k_s^\pm are likely to suffer from oscillation, but larger k_s^\pm can decrease the accuracy. After attempts, k_s is set as 1/28 for the Graphite and NCM electrode, and 1/9 for the LFPO electrode. However, oscil-

lations still exist for the LFPO cell when it is exhausted (very low SOC) in a high ambient temperature. Although oscillations are not found for other scenarios or for the NCM cell, a stabilizing algorithm is still necessary for robustness. In this work, the Savitzky-Golay Filter (SGF) [54] is applied to eliminate the oscillation. The SGF can smooth the sequence in a moving-window without resolution loss. Besides, the fitted weights of the moving window are calculated in advance, which makes it high-efficient for online implementations.

Denote the order of SGF by N_{SG} , the moving window length by M_{SG} (M_{SG} should be odd). First the coefficient matrix \mathbf{B} is calculated, its i -th row $\mathbf{B}_{(i,:)} = \left(\mathbf{X} (\mathbf{X}^T \mathbf{X})^{-1} \mathbf{X}^T \mathbf{y}_i \right)^T$, where $\mathbf{X} = [\mathbf{x}^{N_{SG}} \mathbf{x}^{N_{SG}-1} \dots \mathbf{1}]$ and $\mathbf{y}_i = \underbrace{[0 \dots 0]_{i-1}}_{i-1} \underbrace{[1 \ 0 \dots 0]_{M_{SG}-i}}_{M_{SG}-i}$ (\mathbf{x} is $[\frac{1-M_{SG}}{2} \ \frac{3-M_{SG}}{2} \dots -1 \ 0 \ 1 \dots \frac{M_{SG}-3}{2} \ \frac{M_{SG}-1}{2}]^T$). Since The data volume increases steadily in continuous simulation, the SGF is activated when the oscillation is detected and is only applied on the latest M_{SG} data points to reduce computation cost. By experiments, we find that smoothing the $c_{ss}(x_i^\pm, t_k)$, $x = x_1^\pm, \dots, x_4^\pm$ sequences works effectively. Take c_{ss} at x_1^- as an example, the stabilized states are calculated by:

$$\begin{aligned} & [\hat{c}_{ss}(x_1^-, t_{k-M_{SG}+1}) \ \hat{c}_{ss}(x_1^-, t_{k-M_{SG}+2}) \dots \hat{c}_{ss}(x_1^-, t_k)]^T \\ &= \mathbf{B}[c_{ss}(x_1^-, t_{k-M_{SG}+1}) \ c_{ss}(x_1^-, t_{k-M_{SG}+2}) \dots c_{ss}(x_1^-, t_k)]^T. \end{aligned} \quad (51)$$

3.4. Closed-loop correction

In the open-loop manner, the initialization error and iteration error accumulate gradually. It is necessary to correct internal states based on the measurable output. The Kalman Filter theory is widely used in existing research. However, the KF is based on the assumption that the measurement error and process error obey normal distributions. In addition,

there are 19 inertial states in the proposed model and some of them might be unobservable, which brings significant computation burden. By numeric experiments, we find that the voltage error is mainly caused by inaccurate estimations of solid-phase concentrations, a heuristic correction method is designed then.

Suppose the voltage error exceeds a preset threshold at t_k , then the correction is activated. Denote the measured voltage by $\hat{V}(t_k)$, the true OCV is calculated first:

$$OCV(t_k) = \hat{V}(t_k) - \Phi_e(L^+, t_k) + \Phi_e(0^-, t_k) + R_c I(t) - \eta(t_k). \quad (52)$$

where $\eta(t_k)$ (V) is calculated by:

$$\begin{aligned} \eta(t_k) &= F R_f j_n(L^+, t_k) - F R_f j_n(0^-, t_k) \\ &+ \frac{2RT(t_k)}{F} \ln \left(\frac{F j_n(L^+, t_k)}{2i_0(L^+, t_k)} + \sqrt{\left(\frac{F j_n(L^+, t_k)}{2i_0(L^+, t_k)} \right)^2 + 1} \right) \\ &- \frac{2RT(t_k)}{F} \ln \left(\frac{F j_n(0^-, t_k)}{2i_0(0^-, t_k)} + \sqrt{\left(\frac{F j_n(0^-, t_k)}{2i_0(0^-, t_k)} \right)^2 + 1} \right). \end{aligned} \quad (53)$$

Denote the surface stoichiometry at boundaries x_1^- and x_4^+ by $y^-(x_1^-, t_k)$ and $y^+(x_4^+, t_k)$, the correction amount of stoichiometry $\Delta y^+(t_k)$ and $\Delta y^-(t_k)$ can be obtained by solving non-linear equations below:

$$\begin{cases} A^+ L^+ \varepsilon_s^+ c_{s,\max}^+ \Delta y^+(t_k) + A^- L^- \varepsilon_s^- c_{s,\max}^- \Delta y^-(t_k) = 0, \\ f_{OCV}^+(y^+(x_4^+, t_k) + \Delta y^+(t_k)) - f_{OCV}^-(y^-(x_1^-, t_k) + \Delta y^-(t_k)) \\ = OCV(t_k). \end{cases} \quad (54)$$

The first equation of (54) ensures mass conservation of Li^+ . The correction amount of solid-phase concentrations can be

computed by $\Delta c_s^\pm(t_k) = c_{s,\max}^\pm \Delta y^\pm(t_k)$.

Mathematically, the correction is equivalent to adding an instantaneous process to the solid-phase diffusion model, which is proved to be unstable in experiments. Thus, we modify the correction of solid-phase concentrations as a first-order inertial process:

$$dc_s^\pm(t_k) = \exp\left(-\frac{T_{s,k}}{\tau_\Delta^\pm}\right)dc_s^\pm(t_{k-1}) + (1 - \exp\left(-\frac{T_{s,k}}{\tau_\Delta^\pm}\right))\Delta c_s^\pm(t_k). \quad (55)$$

Then the solid-phase concentrations are corrected by:

$$\bar{c}_s(x, t_k) = \bar{c}_s(x, t_k) + dc_s^\pm(t_k), x = x_1^\pm, \dots, x_4^\pm. \quad (56)$$

3.5. The flowchart

The simulation framework is summarized in Algorithm 1.

4. Experimental design and results

Numeric experiments were designed for validation. Our model was compared against two simplified EM models: the ESP model and a high-cited model [21, 40]. The benchmark is a full-order P2D model containing 51 elements for the electrodes and 11 elements for the separator along the x-axis and 18 elements for each particle along the r-axis.

4.1. Designs

Parameter values are listed in Table B.1. The benchmarks are collected from existing research. For varying parameters, coefficients in their expressions are fitted on experimental data as shown in Table 1.

Eight typical operating scenarios covering a wide range of C-rates and temperatures were simulated as listed in Table 2, including constant-current (CC) discharge under different C-rates and temperatures, constant-current and constant-

Algorithm 1 Simulation steps

Require: Manufacturing and material information.

- 1: Set parameters in Table B.1.
- 2: Set cut-off voltages, solve operating regions via (47).
- 3: Obtain the SOC-OCV curve via (48).
- 4: Measure the battery OCV and ambient temperature before simulation starts.
- 5: Obtain SOC₀ by interpolation in the SOC-OCV curve.
- 6: Initialize c_{ss} , \bar{c}_s , w via (49), initialize Q_e^\pm via (50), initialize T at the ambient temperature and dc_s at 0.
- 7: **for** each $t = t_1, t_2, \dots, t_N$ **do**
- 8: Acquire the current I and time interval T_s ,
- 9: Update varying parameters D_s , D_e , κ , κ_D and k_r via by (1), (3), (4), (28) and (5),
- 10: Update j_n via (37),
- 11: Update Q_e and c_e via (46) and (11),
- 12: Update \bar{c}_s , w , c_{ss} , dc_s via (46), (56) (23) and (55),
- 13: Update T via (46), update V via (38),
- 14: Measure the battery voltage and temperature.
- 15: **if** Correction is activated **then**
- 16: Update Δc_s via (54),
- 17: Correct T by the measured temperature,
- 18: **else**
- 19: Set $\Delta c_s = 0$,
- 20: **end if**
- 21: **if** Oscillation is detected **then**
- 22: Smooth and update c_{ss} sequences via (51).
- 23: **end if**
- 24: **end for**

Table 1

Fitted coefficients in expressions of D_s , k_r and $\frac{d \ln f_\pm}{d \ln c_e}$.

	LFPO(+)	NCM523(+)	NCM811(+)	Graphite(-)
$E_{A,k_{D_s}}$	0	-7349	-7330	19626
$E_{A,b_{D_s}}$	30011	-313	-309	19626
$k_{D_s,\text{ref}}$	0	-2.05e-14	-2.05e-14	-2.4e-14
$b_{D_s,\text{ref}}$	8e-18	2.65e-14	2.65e-14	2.9e-14
E_{A,k_r}	31997	51997	51997	67995
$k_{r,\text{ref}}$	5.3e-6	2.3e-6	2.6e-6	2.3e-5
PC-EC-DMC				
$\frac{d \ln f_\pm}{d \ln c_e}$	$0.55(c_e/1000)^2 + 1.08(c_e/1000) - 0.44$			

voltage charge under 1 C-rate and 298K (CCCV), alternate charge and discharge under different C-rates and 298K (ACC) and highly random current discharge under 298K (RC). Some current profiles are shown in Fig B.2. The Mean Absolute Error (MAE), Root Mean Squared Error (RMSE) and R-

squared (R^2) are applied for accuracy evaluation:

$$R^2 = 1 - \frac{\sum_{i=1}^N (y_i - \hat{y}_i)^2}{\sum_{i=1}^N (y_i - \bar{y})^2}, MAE = \left(\frac{1}{N} \sum_{i=1}^N |y_i - \hat{y}_i| \right),$$

$$RMSE\% = \sqrt{\frac{1}{N} \sum_{i=1}^N (y_i - \hat{y}_i)^2}.$$
(57)

Table 2

Typical operating scenarios.

No.	-:discharge,+:charge	LFPO	NCM523	NCM811
1	1 C-rate 298K (-)	SOC ₀ =1	SOC ₀ =1	SOC ₀ =1
2	2 C-rate 298K (-)	SOC ₀ =1	SOC ₀ =1	SOC ₀ =1
3	4 C-rate 298K (-)	SOC ₀ =1	SOC ₀ =1	SOC ₀ =1
4	CCCV 298K (+)	SOC ₀ =0	SOC ₀ =0	SOC ₀ =0
5	ACC 298K (±)	SOC ₀ =1	SOC ₀ =0.7	SOC ₀ =0.7
6	RC 298K (-)	SOC ₀ =1	SOC ₀ =1	SOC ₀ =1
7	1 C-rate 273K (-)	SOC ₀ =1	SOC ₀ =1	SOC ₀ =1
8	1 C-rate 313K (-)	SOC ₀ =1	SOC ₀ =1	SOC ₀ =1

The run time of the simplified model and full-order P2D model on a 2.11 GHz Intel Core i5-10210U processor with 16 GB of RAM is given in Table 3. The computation efficiency of the simplified model is validated as expected.

4.2. States monitoring and output prediction

For solution-phase concentrations $c_e(x, t)$, the estimation accuracy is given in Table 4. The final results for each cell are the average of eight scenarios. It is observed that the RMSE and MAE are quite small comparing with the baseline value $c_{e,0} = 1200 \text{ mol/m}^3$, indicating errors are acceptable. The trajectories of $c_e(x, t)$ at x_1^-, \dots, x_4^- in the negative electrode of NCM811 for the ACC and RC scenarios are plotted in Fig 2 as an example.

For reaction rates $j_n(x, t)$, the proposed method is validated on the negative electrode of LFPO, NCM523 and NCM811 cells and the positive electrode of NCM523 and NCM811 cells. The estimation results are compared with the uniform j_n model used in the ESP model and the parabolic poly-

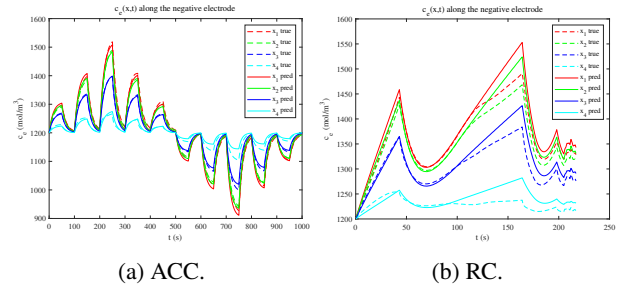


Figure 2: $c_e(x, t)$ in the negative electrode of the NCM811 cell: (a) the ACC scenario. (b) the RC scenario.

mial j_n model used in [21, 40]. As shown in Table 5, the proposed method outperforms the other two significantly. It should be noted that the LiFePO_4 electrode is not simulated due to its too small particle radius. Detail reasons are given in Appendix B.4. The approximated j_n for the NCM523 cell in ACC and RC scenarios are shown in Fig 3 and excellent agreements with the P2D model can be observed, indicating our model is appropriate for dynamic operating conditions.

The normalized values of solid-phase concentrations are chosen for demonstration, i.e., the bulk-averaged Li^+ concentrations are represented by the bulk-averaged solid-phase stoichiometry x_s ($x_s = \bar{c}_s/c_{s,\max}$), the surface Li^+ concentrations are represented by the surface solid-phase stoichiometry x_{ss} ($x_{ss} = c_{ss}/c_{s,\max}$).

Accurate estimation of x_s helps us determine the battery SOC precisely. As shown in Table 6, the proposed model performs better than the other two in general. Interestingly, we find that Han's model (with two first-order processes) or the ESP model (with zero first-order process) performs better for some points, indicating that the number of first-order processes have limited impact on the accuracy. Also, even though for those points, the absolute values of accuracy index of the proposed model are still high enough for practical usage. Thus, we believe that the key for developing solid-phase concentration models is the stabilization, i.e., determining a proper time constant factor is more important than adding more first-order processes. It is worth mentioning

Table 3

The run time (s) for simulations of different cells in various scenarios.

LFPO	1	2	3	4	5	6	7	8
Simulation length	3465	1665.5	768	4194.7	1000	217	3321	3508
P2D	1157.04	634.79	483.24	1393.88	603.45	239.04	585.47	2176.61
Proposed	1.31	1.25	0.96	1.46	1.73	0.72	1.25	1.32
NCM523	1	2	3	4	5	6	7	8
Simulation length	3472	1653.5	762	5261.5	1000	217	3245	3519
P2D	337.98	328.02	256.73	341.10	418.89	162.14	307.37	335.26
Proposed	1.33	1.27	0.98	1.37	1.63	0.65	1.27	1.37
NCM811	1	2	3	4	5	6	7	8
Simulation length	3483	1661.5	767.7	5247.8	1000	217	3277	3528
P2D	343.35	329.85	263.01	344.77	417.47	162.59	330.28	366.18
Proposed	1.36	1.29	1.00	1.39	1.64	0.65	1.29	1.39

Table 4The estimation accuracy of $c_e(x, t)$ for different cells.

	Negative Electrode				Positive Electrode				Separator		
LFPO	1	2	3	4	1	2	3	4	1	2	3
RMSE	19.294	16.816	12.113	12.182	66.354	36.795	34.220	39.391	13.833	12.908	11.744
MAE	16.124	14.097	10.078	9.884	63.037	34.388	27.890	33.160	11.158	10.257	9.268
NCM523	1	2	3	4	1	2	3	4	1	2	3
RMSE	14.537	10.660	4.767	9.147	82.830	46.466	29.666	14.579	10.499	9.655	8.561
MAE	11.905	8.822	4.343	8.088	79.458	44.162	27.835	12.840	9.459	8.552	7.311
NCM811	1	2	3	4	1	2	3	4	1	2	3
RMSE	15.169	11.217	4.405	8.476	82.993	37.941	23.754	11.111	9.758	8.896	7.849
MAE	12.568	9.400	4.039	7.463	79.656	35.973	22.170	9.511	8.782	7.854	6.674

that we have tried the xRA method, Padé approximations and frequency response optimization. Although some methods can perform better in dynamic conditions, they are all found to be likely to suffer from oscillations in the full-cycle simulation. We finally choose to use one first-order process as a trade-off between accuracy, stabilization, and simplicity. Fig 4 plots the x_s at the separator and current collector sides in the negative and positive electrodes of the NCM811 cell

under 1/2/4 C-rate scenarios, it is observed that the results agree well with the P2D model.

Solid-phase surface stoichiometry x_{ss} is the key to estimating reaction rates, predicting SOP, and conducting degradation analysis. The estimation accuracy of x_{ss} is presented in Table 7. It is observed that the proposed model performs better than the other two, especially for the negative electrode. Since side reactions such as SEI generation and lithium

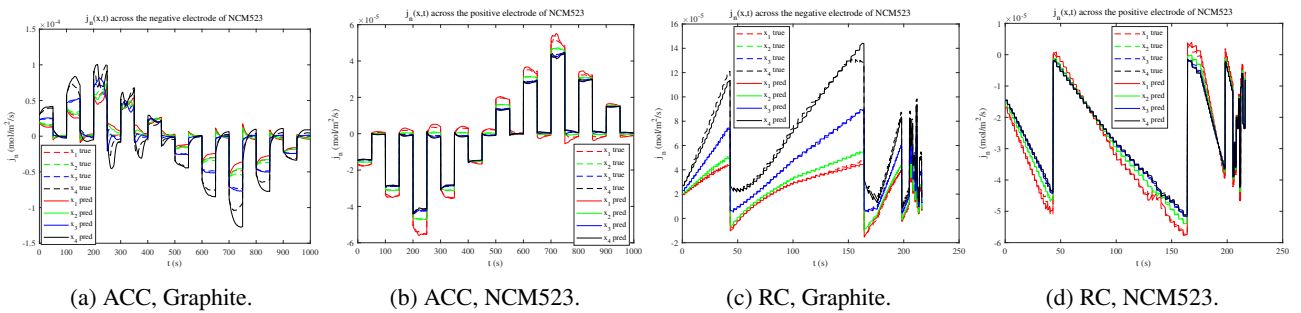


Figure 3: $j_n(x, t)$ for electrodes of the NCM523 cell in different scenarios: (a) The Graphite electrode, ACC. (b) The NCM523 electrode, ACC. (c) The Graphite electrode, RC. (d) The NCM523 electrode, RC.

Table 5The estimation accuracy of $j_n(x, t)$ for different electrodes.

		R ²				RMSE($\times 10^{-7}$)				MAE($\times 10^{-7}$)			
		1	2	3	4	1	2	3	4	1	2	3	4
Graphite(LFPO)	Proposed	0.920	0.932	0.877	0.940	23.0	16.2	15.5	38.4	14.9	10.3	10.5	25.1
	[21, 40]	0.712	0.576	0.128	0.805	41.5	32.9	34.1	63.8	23.5	15.7	15.8	36.8
	Uniform	0.191	0.255	0.349	0.181	58.3	42.4	26.9	116.4	47.5	34.2	22.1	93.4
Graphite(NCM523)	Proposed	0.914	0.931	0.866	0.950	29.2	19.2	22.7	42.4	20.2	13.2	15.4	31.2
	[21, 40]	0.890	0.920	0.831	0.938	35.0	22.0	26.5	47.2	25.9	15.6	19.2	33.1
	Uniform	0.177	0.271	0.342	0.179	80.1	56.4	42.7	147.3	66.6	47.0	36.5	123.7
Graphite(NCM811)	Proposed	0.900	0.921	0.844	0.947	31.0	20.2	23.9	43.1	21.8	14.0	16.4	31.8
	[21, 40]	0.871	0.904	0.799	0.932	37.2	23.3	27.9	48.7	27.8	16.7	20.4	34.5
	Uniform	0.179	0.273	0.343	0.181	80.3	56.5	42.7	147.5	66.8	47.1	36.6	124.0
NCM523	Proposed	0.940	0.772	0.916	0.922	5.70	1.99	2.38	3.00	3.91	1.22	1.55	1.90
	[21, 40]	0.938	0.757	0.915	0.916	6.01	2.10	2.46	3.20	4.10	1.34	1.63	2.08
	Uniform	0.346	0.361	0.357	0.355	19.82	3.74	6.90	9.29	15.8	2.95	5.49	7.36
NCM811	Proposed	0.936	0.684	0.916	0.926	4.44	1.64	1.86	2.23	2.77	0.87	1.08	1.36
	[21, 40]	0.928	0.673	0.908	0.917	4.85	1.75	2.00	2.45	3.05	0.97	1.18	1.52
	Uniform	0.360	0.367	0.365	0.364	15.97	2.82	5.54	7.39	11.17	1.94	3.86	5.11

Table 6The estimation accuracy of solid-phase stoichiometry bulk-averaged $x_s(x, t)$ for different electrodes.

		R ²				RMSE($\times 10^{-4}$)				MAE($\times 10^{-4}$)			
		1	2	3	4	1	2	3	4	1	2	3	4
Graphite(LFPO)	Proposed	0.9952	0.9975	0.9992	0.9973	23.10	17.48	17.24	35.24	18.42	14.23	14.48	27.94
	[21, 40]	0.9905	0.9959	0.9988	0.9954	35.50	25.52	27.72	53.07	27.61	19.22	18.58	39.82
	Uniform	0.9086	0.9553	0.9915	0.8503	212.5	146.9	77.12	381.2	183.8	126.1	66.88	330.7
Graphite(NCM523)	Proposed	0.9879	0.9936	0.9963	0.9901	50.90	38.90	41.37	85.63	43.23	33.53	34.82	68.37
	[21, 40]	0.9712	0.9874	0.9969	0.9923	59.72	43.93	41.96	71.77	49.48	37.52	34.49	55.55
	Uniform	0.7948	0.9256	0.9752	0.7514	396.7	262.6	166.8	693.2	354.4	232.4	153.3	632.4
Graphite(NCM811)	Proposed	0.9913	0.9957	0.9990	0.9944	67.88	53.19	36.34	64.34	57.67	45.76	31.17	51.25
	[21, 40]	0.9813	0.9929	0.9986	0.9947	69.15	51.73	43.50	66.10	58.65	44.90	36.59	51.43
	Uniform	0.7485	0.9026	0.9844	0.7719	417.3	282.5	144.5	671.3	375.7	253.2	129.0	607.1
NCM523	Proposed	0.9978	0.9974	0.9972	0.9971	26.78	25.98	24.73	25.40	26.24	25.64	24.38	24.96
	[21, 40]	0.9983	0.9974	0.9971	0.9969	21.13	25.82	25.96	26.64	20.83	25.50	25.58	26.17
	Uniform	0.9957	0.9983	0.9935	0.9914	67.24	17.48	49.42	59.67	57.40	16.67	46.64	55.60
NCM811	Proposed	0.9979	0.9972	0.9968	0.9964	27.57	29.12	30.07	31.48	27.32	28.88	29.75	31.09
	[21, 40]	0.9982	0.9972	0.9967	0.9963	24.56	29.01	30.71	32.12	24.35	28.77	30.37	31.71
	Uniform	0.9969	0.9982	0.9931	0.9911	38.65	22.31	44.94	50.70	35.79	22.09	43.72	48.91

plating mainly occur in negative electrodes, a higher accuracy of estimating x_{ss} is pivotal. Fig 5 plots the x_{ss} at the separator and current collector in the negative and positive electrodes of the NCM811 cell in 298/273/313K scenarios, the results are coincident with the P2D model.

Prediction accuracy of the terminal voltage is given in

Table 8, three models can all achieve high accuracy while the proposed model performs better in general. Terminal voltages of the NCM523 cell and LFPO cell in some scenarios are plotted in Fig 6. (The performance of the NCM811 cell is similar to the NCM523 cell and are not given to save space.)

However, it is observed that in dynamic currents, e.g., the

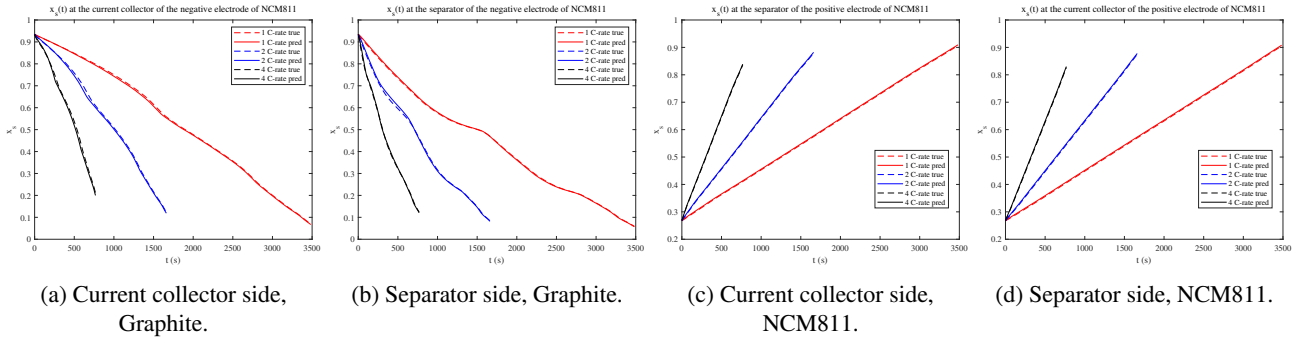


Figure 4: $x_s(x, t)$ at different positions in electrodes of the NCM811 cell under constant-current discharge: (a) Current collector side, Graphite, (b) Separator side, Graphite, (c) Current collector side, NCM811, (d) Separator side, NCM811.

Table 7

The estimation accuracy of solid-phase surface stoichiometry $x_{ss}(x, t)$ for different electrodes.

	R^2				$RMSE(\times 10^{-4})$				$MAE(\times 10^{-4})$			
	1	2	3	4	1	2	3	4	1	2	3	4
Graphite(LFPO)												
Proposed	0.9688	0.9731	0.9777	0.9761	80.05	75.01	79.75	120.2	55.22	52.41	59.37	91.10
[21, 40]	0.9520	0.9631	0.9748	0.9733	105.2	93.79	100.6	134.4	70.83	62.06	64.69	101.9
Uniform	0.3102	0.4429	0.7719	0.7696	420.5	354.2	263.92	518.6	338.9	280.1	212.4	421.7
Graphite(NCM523)												
Proposed	0.9319	0.9454	0.9587	0.9493	165.4	160.1	177.1	253.8	124.9	118.8	121.5	158.6
[21, 40]	0.8803	0.9168	0.9529	0.9458	197.0	183.9	187.9	263.5	152.2	137.8	126.8	171.6
Uniform	-2.1964	-1.1228	0.3186	0.5626	949.8	830.5	653.3	926.6	737.7	607.4	481.4	773.7
Graphite(NCM811)												
Proposed	0.9392	0.9510	0.9626	0.9533	170.8	162.7	172.2	240.9	130.6	121.6	120.6	153.7
[21, 40]	0.8930	0.9265	0.9576	0.9493	197.2	181.9	182.3	253.8	155.1	138.3	127.1	172.6
Uniform	-2.1919	-1.1150	0.3289	0.5756	952.4	831.5	646.5	913.6	746.5	614.5	468.6	757.7
NCM523												
Proposed	0.9932	0.9934	0.9935	0.9934	29.27	29.28	30.20	30.39	24.00	24.80	25.60	25.68
[21, 40]	0.9928	0.9928	0.9927	0.9927	32.12	31.04	31.76	31.94	27.33	26.22	26.79	26.82
Uniform	0.9561	0.9544	0.9461	0.9432	114.7	61.57	84.00	93.55	96.22	47.95	73.13	82.58
NCM811												
Proposed	0.9943	0.9940	0.9936	0.9934	32.46	32.79	33.25	33.57	27.10	27.83	28.33	28.59
[21, 40]	0.9938	0.9934	0.9930	0.9927	35.05	34.61	34.96	35.20	29.54	29.34	29.69	29.87
Uniform	0.9627	0.9608	0.9527	0.9500	82.19	63.23	79.76	85.04	69.82	48.14	68.89	74.22

ACC and RC scenarios, the prediction error is likely to increase. Thus, a closed-loop correction framework is necessary for practical implementations.

4.3. Closed-loop corrections for online controlling

Although the states monitoring and output prediction agree well with the full-order P2D model, a closed-loop framework is necessary for real-world applications since the initialization error and the model error will accumulate in continuous run and oscillations may occur under some extreme conditions.

4.3.1. Eliminate the oscillation

We observe that for the LFPO cell in the 1 C-rate 313K scenario, both our model and Han's model oscillate at the end of discharge, as shown in Fig 7a. We speculate that it may be caused by the sharp gradient of the U_{OCP} when the battery is exhausted, as shown in Fig B.1. Once the oscillation is detected, the SGF is activated on the $c_{ss}(x_i^\pm, t_k)$ sequences and the oscillation can be eliminated effectively as shown in Fig 7b. In this work, N_{SG} is set as 2 and M_{SG} is set as 49.

Applied Energy

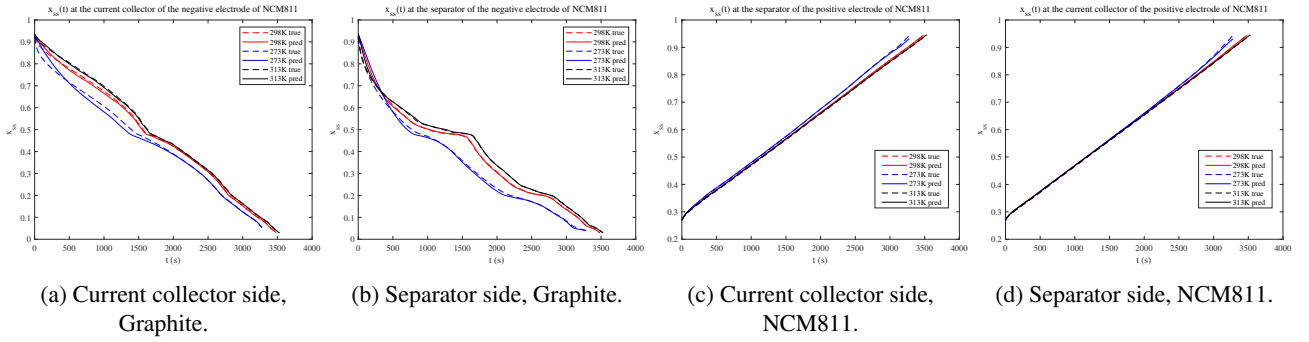


Figure 5: $x_{ss}(x, t)$ at different positions in electrodes of the NCM811 cell under different temperatures discharge: (a) Current collector side, Graphite, (b) Separator side, Graphite, (c) Current collector side, NCM811, (d) Separator side, NCM811.

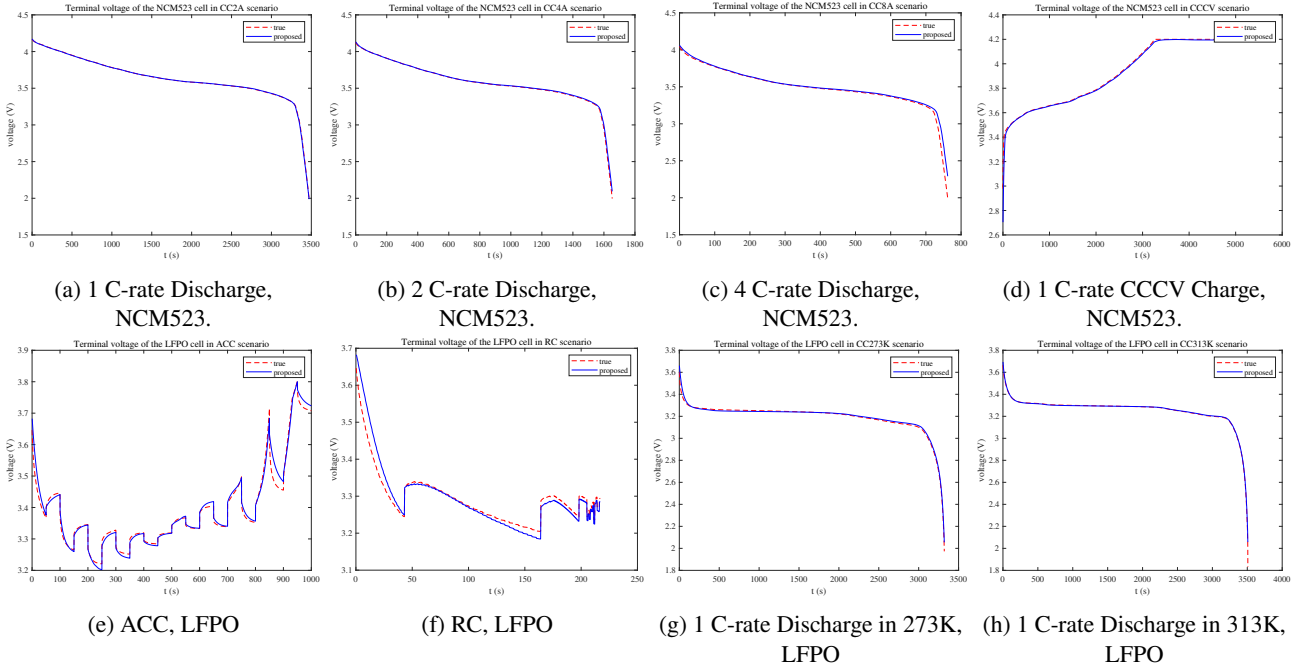


Figure 6: $V(t)$ of different cells under different scenarios: (a) 1 C-rate Discharge, NCM523, (b) 2 C-rate Discharge, NCM523, (c) 4 C-rate Discharge, NCM523, (d) 1 C-rate CCCV Charge, NCM523, (e) ACC, LFPO, (f) RC, LFPO, (g) 1 C-rate Discharge in 273K, LFPO, (h) 1 C-rate Discharge in 313K, LFPO.

4.3.2. Correct the terminal voltage

For the NCM cell, the prediction of $V(t)$ is less accurate:

(a) at the end of the 4 C-rate discharge and 1 C-rate 273K discharge scenarios, (b) in the ACC and RC scenarios. For the LFPO cell, the prediction of $V(t)$ is less accurate in ACC and

RC scenarios. For above mentioned scenarios, the proposed closed-loop correction is applied to track the measured voltage. Once the terminal voltage error is higher than a given threshold, the correction is activated. The prediction accuracy of $V(t)$ in closed-loop simulation is given in Table 9

Table 8

The prediction accuracy of the terminal voltage for different cells.

		LFPO			NCM523			NCM811	
	Proposed	[21, 40]	ESP	Proposed	[21, 40]	ESP	Proposed	[21, 40]	ESP
R2	0.979	0.983	0.953	0.983	0.974	0.949	0.992	0.984	0.955
RMSE	0.01371	0.01536	0.02143	0.02459	0.03023	0.02636	0.01995	0.02499	0.02323
MAE	0.00774	0.00927	0.01205	0.00843	0.01617	0.01859	0.00771	0.01456	0.01629

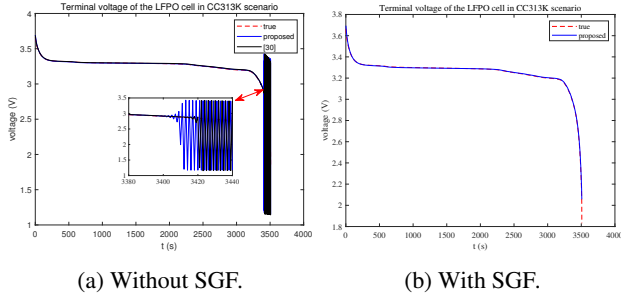


Figure 7: $V(t)$ of the LFPO cell in the 1 C-rate 313K scenario: (a) without SGF, (b) with SGF.

Table 9

R^2 of $V(t)$ in closed-loop simulations.

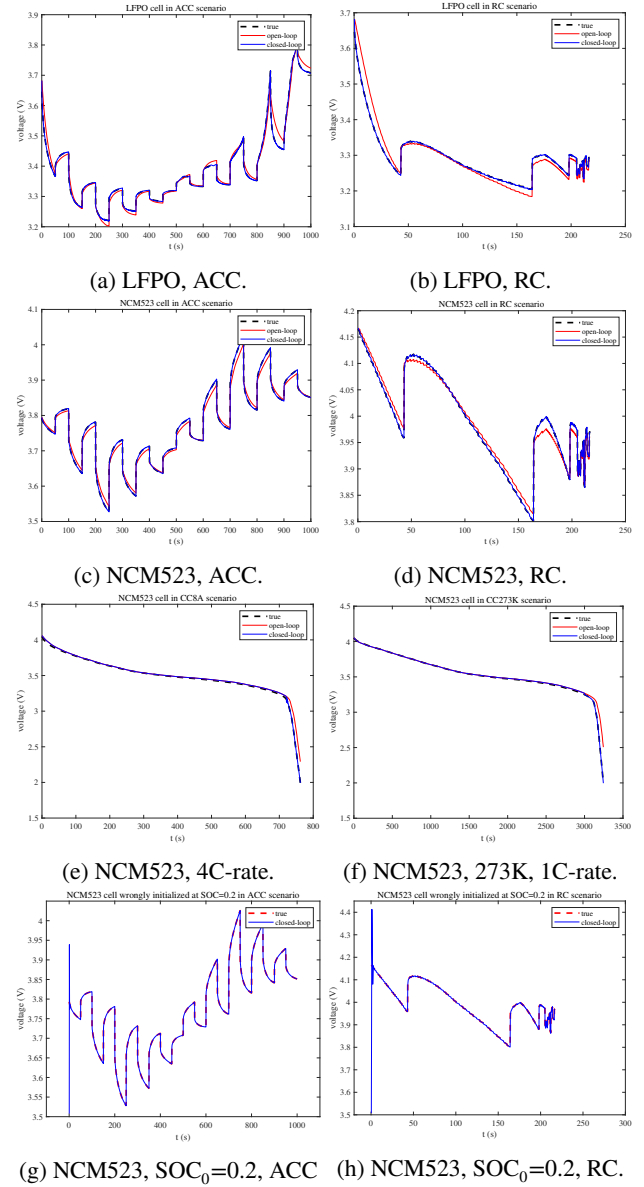
voltage R^2	LFPO ACC	LFPO RC	NCM CC8A
opne-loop	0.9843	0.8916	0.9673
closed-loop	0.9999	0.9996	0.9986
voltage R^2	NCM CC273K	NCM ACC	NCM RC
opne-loop	0.9440	0.9939	0.9828
closed-loop	0.9999	0.9998	0.9995

and shown in Fig 8. It is observed that the voltage trajectory can be effectively corrected in the closed-loop manner. Since the voltage error is assumed to be totally attributed to solid-phase concentrations when designing the correction method, it will decrease the states estimation accuracy somehow. Thus, the correction is only activated when the voltage deviation is quite large to achieve a trade-off between the output accuracy and internal states accuracy.

For the simulation with wrong initialized internal states, the closed-loop corrections can help the system quickly converge to the correct values as shown in Fig 8(g),(h), where the initial SOC in ACC and RC scenarios are both set as 0.2 (the true values are 0.7 for each).

5. Conclusions

This paper proposes a simplified electro-chemical model and a simulation framework for lithium-ion battery cells, enabling precise in-situ monitoring of internal states and convenient online controlling of the battery. Numeric experiments of different batteries in various scenarios demonstrate the effectiveness and efficiency of this work. For future re-



(g) NCM523, $SOC_0=0.2$, ACC (h) NCM523, $SOC_0=0.2$, RC.

Figure 8: $V(t)$ in closed-loop simulations: (a) the LFPO cell in ACC scenario, (b) the LFPO cell in RC scenario, (c) the NCM523 cell in ACC scenario, (d) the NCM523 cell in RC scenario, (e) the NCM523 cell in 4C-rate discharge scenario, (f) the NCM523 cell in 273K 1C-rate discharge scenario, (g) the NCM523 cell with wrong $SOC_0=0.2$ in ACC scenario, (h) the NCM523 cell with wrong $SOC_0=0.2$ in RC scenario.

search, we will develop the specific parameter estimation algorithm for the proposed model.

A. List of symbols

A.1. Geometric parameters

m the weight of the battery cell kg;

$L^{\pm,sep}$ the thickness of positive electrode (+), negative

electrode (–) and separator (sep) m;

$A^{\pm,sep}$ the projected area of positive electrode (+), negative electrode (–) and separator (sep) m²;

A_s the surface area of the battery cell m²;

A.2. Transport parameters

D_s the effective solid phase diffusion coefficient m²/s;

D_e the effective solution phase diffusion coefficient m²/s;

σ_s the solid phase electronic conductivity S/m;

κ the solution phase ionic conductivity S/m;

t_+^0 the transference number dimensionless;

R_c the contact resistance of the current collector Ω ;

R_f^{\pm} the resistance of the CEI/SEI film $\Omega \cdot m^2$;

A.3. Material parameters

R_s^{\pm} the radius of particles of active materials in the positive electrode (+) and negative electrode (–) m;

a_s^{\pm} the specific surface area of particles of active materials in the positive electrode (+) and negative electrode (–) 1/m;

M^{\pm} the molar mass of active materials in the positive electrode (+) and negative electrode (–) kg/mol;

ρ^{\pm} the density of active materials in the positive electrode (+) and negative electrode (–) kg/m³;

$c_{s,max}^{\pm}$ the maximum concentration of lithium-ions in active materials in the positive electrode (+) and negative electrode (–) mol/m³;

$\epsilon_e^{\pm,sep}$ the porosity of the positive electrode (+), negative electrode (–) and separator (sep) dimensionless;

ϵ_s^{\pm} the volume fraction of the positive electrode (+) and negative electrode (–) dimensionless;

$c_{e,0}$ the average electrolyte Li⁺ concentration mol/m³;

A.4. Thermal parameters

C_p the heat capacity of the battery cell J/kg/K;

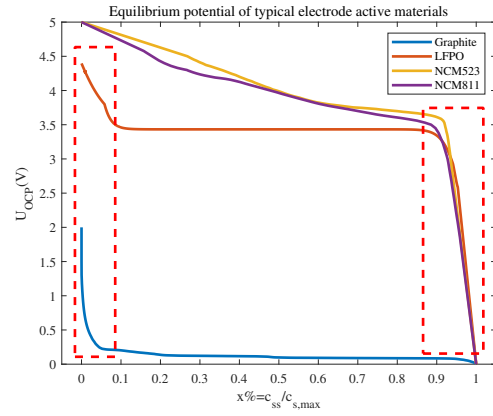


Figure B.1: Equilibrium potential of typical electrode active materials.

h_c the heat transfer coefficient of the battery cell W/m²/K;

k_r^{\pm} the reaction rate coefficient of the active material of the positive electrode (+) and negative electrode (–)

A·m^{2.5}/mol^{1.5};

A.5. Constant parameters

F Faraday constant C/mol;

R Gas constant J/mol/K;

p the Bruggeman coefficient dimensionless;

k_s^{\pm} the correction factor of the time constant for the first-order process of diffusion in the active material of the positive electrode (+) and negative electrode (–) dimensionless;

B. Supplemental material

B.1. Parameter settings

Parameter settings of the lithium-ion battery cells tested in this work are given in Table B.1.

B.2. Equilibrium potential

Equilibrium potential curves of typical electrode active materials (Graphite, LFPO, NCM523 and NCM811) are shown in Fig B.1.

Table B.1

Parameter settings of the lithium-ion battery cell used in this work.

Parameters	Benchmark	Set values
$^m m$	-	LFPO: 3.69×10^{-2} , NCM523: 3.95×10^{-2} , NCM811: 3.85×10^{-2}
$^m L^+$	-	7.75×10^{-5}
$^m L^-$	-	8.1×10^{-5}
$^m L^{\text{sep}}$	-	2×10^{-5}
$^m A^+$	-	6.1×10^{-2}
$^m A^-$	-	6.41×10^{-2}
$^m A^{\text{sep}}$	-	6.36×10^{-2}
$^m A_s$	-	4.4×10^{-3}
$^f D_s^+$	LFPO: 1.25×10^{-15} [48], NCM: $1-10 \times 10^{-14}$ [8, 10, 43, 55]	(1)
$^f D_s^-$	C: 3.9×10^{-14} – 5.5×10^{-14} [17, 20, 41, 47, 48, 52]	(1)
$^f D_e$	$2.6-7.5 \times 10^{-10}$ [17, 21, 32, 41, 43, 47, 52]	(3)
$^a \sigma_s^+$	LFPO: 10.8 [48], NCM: 1-68 [8, 26, 43, 56]	LFPO&NCM523&NCM811: 3.8
$^a \sigma_s^-$	100 [8, 17, 20, 32, 41, 47, 52]	100
$^f \kappa$	3.46 [24]	(4)
$^c t_+^0$	0.36-0.4 [32, 43, 47, 48, 57]	0.38
$^a R_c$	-	0.0064
$^a R_f^+$	0	1.3×10^{-4}
$^a R_f^-$	0.001-0.1 [43, 55, 56]	3.3×10^{-4}
$^a R_s^+$	LFPO: $0.2-1.7 \times 10^{-7}$ [48], NCM: $1-18 \times 10^{-6}$ [10, 43, 55, 57]	LFPO: 5.2×10^{-8} , NCM523&NCM811: 5×10^{-6}
$^a R_s^-$	$1-12.5 \times 10^{-6}$ [8, 17, 20, 21, 41, 47, 48, 52]	7.5×10^{-6}
$^c M^+$	LFPO: 157.7×10^{-3} , NCM523: 96.5×10^{-3} , NCM811: 97.3×10^{-3}	LFPO: 157.7×10^{-3} , NCM523: 96.5×10^{-3} , NCM811: 97.3×10^{-3}
$^c M^-$	72.06×10^{-3}	72.06×10^{-3}
$^c \rho^+$	LFPO: 3.6×10^3 , NCM523&NCM811: 4.8×10^3	LFPO: 3.6×10^3 , NCM523&NCM811: 4.8×10^3
$^c \rho^-$	2.24×10^3	2.24×10^3
$^c c_{s,\text{max}}^+$	ρ^+ / M^+	LFPO: 2.28×10^4 , NCM523: 4.97×10^4 , NCM811: 4.93×10^4
$^c c_{s,\text{max}}^-$	ρ^- / M^-	3.11×10^4
$^m \epsilon_e^+$	0.27-0.45 [43, 55]	LFPO: 0.4461, NCM523: 0.4401, NCM811: 0.5038
$^m \epsilon_e^-$	0.26-0.5 [43, 55]	LFPO: 0.4733, NCM523: 0.4893, NCM811: 0.4893
$^m \epsilon_e^{\text{sep}}$	0.4-0.55 [43, 55]	0.4
$^m \epsilon_s^+$	0.35-0.5 [43, 55]	LFPO: 0.4928, NCM523: 0.4806, NCM811: 0.4258
$^m \epsilon_s^-$	0.4-0.5 [43, 55]	LFPO: 0.489, NCM523: 0.4742, NCM811: 0.4742
$^a a_s^+$	$3\epsilon_s^+ / R_s^+$	LFPO: 2.84×10^7 , NCM523: 2.88×10^5 , NCM811: 2.56×10^5
$^a a_s^-$	$3\epsilon_s^- / R_s^-$	LFPO: 1.96×10^5 , NCM523: 1.90×10^5 , NCM811: 1.90×10^5
$^m c_{e,0}$	1000-1200 [17, 32, 20, 21, 41, 47]	1200
$^a C_p$	746-998 [23, 52]	1000
$^a h_c$	5-20 [17, 23]	20
$^f k_r^+$	LFPO: 9.65×10^{-8} [48], NCM: $9.65-96.5 \times 10^{-7}$ [43, 55]	(5)
$^f k_r^-$	$1.7-9.6 \times 10^{-6}$ [43, 17, 20, 41, 47]	(5)
$^c p$	1.5-4.1 [17, 20, 21, 47, 48]	1.5
$^a k_s^+$	-	LFPO: 1/9, NCM523: 1/28, NCM811: 1/28
$^a k_s^-$	-	1/28
$^c F$	96485.33	96485.33
$^c R$	8.314	8.314

^a: Assumed.^c: Constant values.^f: Fitted by material properties.^m: Manufactured.

B.3. Battery current

Some typical currents of different operation scenarios for testing in this work are shown in Fig B.2.

B.4. Reaction rate distribution of LiFePO₄

The particle radius of LiFePO₄ is about 100 times smaller than the NCM and graphite, which induces the peak of reaction rates across the electrode very narrow and high. Since we only select 4 points along the x-axis for simplicity, such

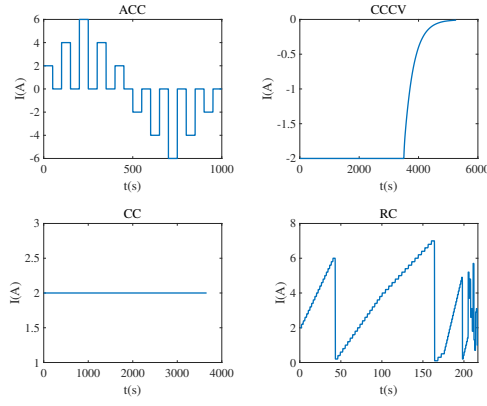


Figure B.2: Current profiles of four typical operation scenarios.

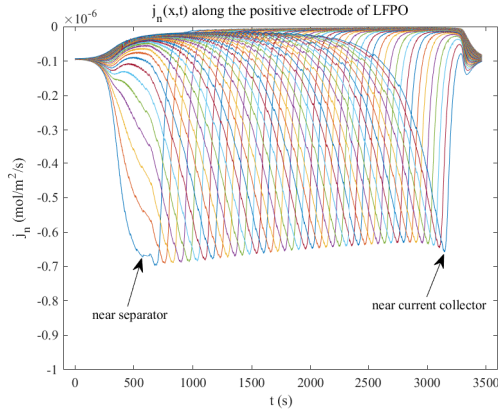


Figure B.3: The reaction rate distribution across the LFPO electrode.

granularity is inapplicable for capturing the extremely uneven distribution characteristics of j_n for the LiFePO_4 electrode. However, we can observe from Fig B.3 that within a full-cycle operation, the peak of $j_n(x, t)$ moves steadily from the separator to the current collector and $\int_{t_0}^T j_n(x, t) dt$ for every point on the x-axis are almost the same. Actually, when we conduct the degradation analysis, we focus more on the integration of $j_n(x, t)$ within a specific time period rather than its instantaneous values. Thus, the uniform distribution of j_n is applied for the LiFePO_4 electrode in this work.

References

- [1] S. Li, H. He, J. Li, Big data driven lithium-ion battery modeling method based on SDAE-ELM algorithm and data pre-processing technology, *Applied Energy* 242 (2019) 1259–1273.
- [2] X. Hu, S. Li, H. Peng, A comparative study of equivalent circuit models for Li-ion batteries, *Journal of Power Sources* 198 (2012) 359–367.
- [3] X. Hu, R. Xiong, B. Egardt, Model-Based Dynamic Power Assessment of Lithium-Ion Batteries Considering Different Operating Conditions, *IEEE Transactions on Industrial Informatics* 10 (2014) 1948–1959. Conference Name: IEEE Transactions on Industrial Informatics.
- [4] X. Ding, D. Zhang, J. Cheng, B. Wang, P. C. K. Luk, An improved Thevenin model of lithium-ion battery with high accuracy for electric vehicles, *Applied Energy* 254 (2019) 113615.
- [5] M. Doyle, T. F. Fuller, J. Newman, Modeling of galvanostatic charge and discharge of the lithium/polymer/insertion cell, *Journal of The Electrochemical Society* 140 (1993) 1526–1533.
- [6] N. Legrand, S. Raël, B. Knosp, M. Hinaje, P. Desprez, F. Lapique, Including double-layer capacitance in lithium-ion battery mathematical models, *Journal of Power Sources* 251 (2014) 370–378.
- [7] Z. Chu, G. L. Plett, M. S. Trimboli, M. Ouyang, A control-oriented electrochemical model for lithium-ion battery, Part I: Lumped-parameter reduced-order model with constant phase element, *Journal of Energy Storage* 25 (2019) 100828.
- [8] Q. Zhang, D. Wang, B. Yang, X. Cui, X. Li, Electrochemical model of lithium-ion battery for wide frequency range applications, *Electrochimica Acta* 343 (2020) 136094.
- [9] M. Farkhondeh, C. Delacourt, Mathematical Modeling of Commercial LiFePO_4 Electrodes Based on Variable Solid-State Diffusivity, *Journal of The Electrochemical Society* 159 (2011) A177–A192.
- [10] Y. Gao, C. Zhu, X. Zhang, B. Guo, Implementation and evaluation of a practical electrochemical-thermal model of lithium-ion batteries for EV battery management system, *Energy* 221 (2021) 119688.
- [11] R. Xiong, L. Li, Z. Li, Q. Yu, H. Mu, An electrochemical model based degradation state identification method of Lithium-ion battery for all-climate electric vehicles application, *Applied Energy* 219 (2018) 264–275.
- [12] C. M. Doyle, Design and simulation of lithium rechargeable batteries, Lawrence Berkeley National Laboratory (2010).
- [13] F. Ringbeck, M. Garbade, D. U. Sauer, Uncertainty-aware state estimation for electrochemical model-based fast charging control of lithium-ion batteries, *Journal of Power Sources* 470 (2020) 228221.
- [14] M. G. Hennessy, I. R. Moyses, Asymptotic reduction and homoge-

- nization of a thermo-electrochemical model for a lithium-ion battery, *Applied Mathematical Modelling* 80 (2020) 724–754.
- [15] L. Cai, R. E. White, Reduction of model order based on proper orthogonal decomposition for lithium-ion battery simulations, *Journal of The Electrochemical Society* 156 (2009) A154.
- [16] Y. Zhao, S.-Y. Choe, J. Kee, Modeling of degradation effects and its integration into electrochemical reduced order model for Li(mnco)O₂/graphite polymer battery for real time applications, *Electrochimica Acta* 270 (2018) 440–452.
- [17] C. Zou, C. Manzie, D. Nesic, A Framework for Simplification of PDE-Based Lithium-Ion Battery Models, *IEEE Transactions on Control Systems Technology* 24 (2016) 1594–1609.
- [18] C. Lyu, Y. Song, J. Zheng, W. Luo, G. Hinds, J. Li, L. Wang, In situ monitoring of lithium-ion battery degradation using an electrochemical model, *Applied Energy* 250 (2019) 685–696.
- [19] Y. Hu, Y. Yin, Y. Bi, S.-Y. Choe, A control oriented reduced order electrochemical model considering variable diffusivity of lithium ions in solid, *Journal of Power Sources* 468 (2020) 228322.
- [20] S. Khaleghi Rahimian, S. Rayman, R. E. White, Extension of physics-based single particle model for higher charge–discharge rates, *Journal of Power Sources* 224 (2013) 180–194.
- [21] X. Han, M. Ouyang, L. Lu, J. Li, Simplification of physics-based electrochemical model for lithium ion battery on electric vehicle. Part I: Diffusion simplification and single particle model, *Journal of Power Sources* 278 (2015) 802–813.
- [22] L. Wu, K. Liu, H. Pang, Evaluation and observability analysis of an improved reduced-order electrochemical model for lithium-ion battery, *Electrochimica Acta* 368 (2021) 137604.
- [23] D. Wang, H. Huang, Z. Tang, Q. Zhang, B. Yang, B. Zhang, A lithium-ion battery electrochemical–thermal model for a wide temperature range applications, *Electrochimica Acta* 362 (2020) 137118.
- [24] C. Li, N. Cui, C. Wang, C. Zhang, Reduced-order electrochemical model for lithium-ion battery with domain decomposition and polynomial approximation methods, *Energy* 221 (2021) 119662.
- [25] Y. Li, M. Vilathgamuwa, S. S. Choi, T. W. Farrell, N. T. Tran, J. Teague, Development of a degradation-conscious physics-based lithium-ion battery model for use in power system planning studies, *Applied Energy* 248 (2019) 512–525.
- [26] Y. Bi, S.-Y. Choe, An adaptive sigma-point Kalman filter with state equality constraints for online state-of-charge estimation of a Li(NiMnCo)O₂/Carbon battery using a reduced-order electrochemical model, *Applied Energy* 258 (2020) 113925.
- [27] G. Fan, Systematic parameter identification of a control-oriented electrochemical battery model and its application for state of charge estimation at various operating conditions, *Journal of Power Sources* 470 (2020) 228153.
- [28] T.-S. Dao, C. P. Vyasarayani, J. McPhee, Simplification and order reduction of lithium-ion battery model based on porous-electrode theory, *Journal of Power Sources* 198 (2012) 329–337.
- [29] J. Li, D. Wang, L. Deng, Z. Cui, C. Lyu, L. Wang, M. Pecht, Aging modes analysis and physical parameter identification based on a simplified electrochemical model for lithium-ion batteries, *Journal of Energy Storage* 31 (2020) 101538.
- [30] J. C. Forman, S. Bashash, J. L. Stein, H. K. Fathy, Reduction of an electrochemistry-based Li-ion battery model via quasi-linearization and Padé approximation, *Journal of The Electrochemical Society* 158 (2011) A93.
- [31] Z. Deng, X. Hu, X. Lin, L. Xu, J. Li, W. Guo, A reduced-order electrochemical model for all-solid-state batteries, *IEEE Transactions on Transportation Electrification* 7 (2021) 464–473.
- [32] K. A. Smith, C. D. Rahn, C.-Y. Wang, Control oriented 1D electrochemical model of lithium ion battery, *Energy Conversion and Management* 48 (2007) 2565–2578.
- [33] X. Li, G. Fan, K. Pan, G. Wei, C. Zhu, G. Rizzoni, M. Canova, A physics-based fractional order model and state of energy estimation for lithium ion batteries. Part I: Model development and observability analysis, *Journal of Power Sources* 367 (2017) 187–201.
- [34] F. Feng, S. Teng, K. Liu, J. Xie, Y. Xie, B. Liu, K. Li, Co-estimation of lithium-ion battery state of charge and state of temperature based on a hybrid electrochemical-thermal-neural-network model, *Journal of Power Sources* 455 (2020) 227935.
- [35] J. L. Lee, A. Chemistruck, G. L. Plett, One-dimensional physics-based reduced-order model of lithium-ion dynamics, *Journal of Power Sources* 220 (2012) 430–448.
- [36] R. Klein, N. A. Chaturvedi, J. Christensen, J. Ahmed, R. Findeisen, A. Kojic, Electrochemical Model Based Observer Design for a Lithium-Ion Battery, *IEEE Transactions on Control Systems Technology* 21 (2013) 289–301.
- [37] X. Hu, S. Stanton, L. Cai, R. E. White, A linear time-invariant model for solid-phase diffusion in physics-based lithium ion cell models, *Journal of Power Sources* 214 (2012) 40–50.
- [38] Y. Wang, M. Li, Z. Chen, Experimental study of fractional-order

- models for lithium-ion battery and ultra-capacitor: Modeling, system identification, and validation, *Applied Energy* 278 (2020) 115736.
- [39] Z. Deng, L. Yang, H. Deng, Y. Cai, D. Li, Polynomial approximation pseudo-two-dimensional battery model for online application in embedded battery management system, *Energy* 142 (2018) 838–850.
- [40] X. Han, M. Ouyang, L. Lu, J. Li, Simplification of physics-based electrochemical model for lithium ion battery on electric vehicle. Part II: Pseudo-two-dimensional model simplification and state of charge estimation, *Journal of Power Sources* 278 (2015) 814–825.
- [41] W. Luo, C. Lyu, L. Wang, L. Zhang, A new extension of physics-based single particle model for higher charge–discharge rates, *Journal of Power Sources* 241 (2013) 295–310.
- [42] D. Li, L. Yang, C. Li, Control-oriented thermal-electrochemical modeling and validation of large size prismatic lithium battery for commercial applications, *Energy* 214 (2021) 119057.
- [43] W. Li, Y. Fan, F. Ringbeck, D. Jöst, X. Han, M. Ouyang, D. U. Sauer, Electrochemical model-based state estimation for lithium-ion batteries with adaptive unscented Kalman filter, *Journal of Power Sources* 476 (2020) 228534.
- [44] V. R. Subramanian, V. Boovaragavan, V. Ramadesigan, M. Arabandi, Mathematical model reformulation for lithium-ion battery simulations: Galvanostatic boundary conditions, *Journal of The Electrochemical Society* 156 (2009) A260.
- [45] A. Allam, S. Onori, Online Capacity Estimation for Lithium-Ion Battery Cells via an Electrochemical Model-Based Adaptive Interconnected Observer, *IEEE Transactions on Control Systems Technology* (2020) 1–16. Conference Name: IEEE Transactions on Control Systems Technology.
- [46] L. O. Valo, J. N. Reimers, Transport properties of LiPF₆-based li-ion battery electrolytes, *Journal of The Electrochemical Society* 152 (2005) A882.
- [47] M. Torchio, L. Magni, R. B. Gopaluni, R. D. Braatz, D. M. Raimondo, LIONSIMBA: A Matlab Framework Based on a Finite Volume Model Suitable for Li-Ion Battery Design, Simulation, and Control, *Journal of The Electrochemical Society* 163 (2016) A1192–A1205.
- [48] M. Xu, R. Wang, P. Zhao, X. Wang, Fast charging optimization for lithium-ion batteries based on dynamic programming algorithm and electrochemical-thermal-capacity fade coupled model, *Journal of Power Sources* 438 (2019) 227015.
- [49] K. E. Thomas, J. Newman, R. M. Darling, Mathematical Modeling of Lithium Batteries, in: W. A. van Schalkwijk, B. Scrosati (Eds.), *Advances in Lithium-Ion Batteries*, Springer US, Boston, MA, 2002, pp. 345–392.
- [50] D. Noren, M. Hoffman, Clarifying the Butler–Volmer equation and related approximations for calculating activation losses in solid oxide fuel cell models, *Journal of Power Sources* 152 (2005) 175–181.
- [51] L. Rao, J. Newman, Heat-generation rate and general energy balance for insertion battery systems, *Journal of The Electrochemical Society* 144 (1997) 2697–2704.
- [52] G. G. Botte, B. A. Johnson, R. E. White, Influence of Some Design Variables on the Thermal Behavior of a Lithium-Ion Cell, *Journal of The Electrochemical Society* 146 (1999) 914–923.
- [53] W. B. Gu, C. Y. Wang, Thermal-Electrochemical Modeling of Battery Systems, *Journal of The Electrochemical Society* 147 (2000) 2910.
- [54] W. H. Press, S. A. Teukolsky, Savitzky-golay smoothing filters, *Computers in Physics* 4 (1990) 669–672.
- [55] W. Li, D. Cao, D. Jöst, F. Ringbeck, M. Kuipers, F. Frie, D. U. Sauer, Parameter sensitivity analysis of electrochemical model-based battery management systems for lithium-ion batteries, *Applied Energy* 269 (2020) 115104.
- [56] Y. Yin, Y. Hu, S.-Y. Choe, H. Cho, W. T. Joe, New fast charging method of lithium-ion batteries based on a reduced order electrochemical model considering side reaction, *Journal of Power Sources* 423 (2019) 367–379.
- [57] X. Zhao, Y. Yin, Y. Hu, S.-Y. Choe, Electrochemical-thermal modeling of lithium plating/stripping of Li(Ni_{0.6}Mn_{0.2}Co_{0.2})O₂/Carbon lithium-ion batteries at subzero ambient temperatures, *Journal of Power Sources* 418 (2019) 61–73.